Scientific Reports

https://doi.org/10.1038/s41598-026-37671-z

Article in Press

Zn-based metal organic frameworks encapsuated cauliflower leaves-derived biochar composite for photocatalytic removal of victoria blue and crystal violet

Received: 15 August 2025

Accepted: 23 January 2026

Published online: 04 February 2026

Cite this article as: Darabdhara J., Hazarika B. & Ahmaruzzaman M. Zn-based metal organic frameworks encapsuated cauliflower leaves-derived biochar composite for photocatalytic removal of victoria blue and crystal violet. *Sci Rep* (2026). https://doi.org/10.1038/s41598-026-37671-z

Jnyanashree Darabdhara, Berileena Hazarika & Mohammed Ahmaruzzaman

Zn-based Metal Organic Frameworks encapsuated Cauliflower leaves-derived Biochar composite for Photocatalytic removal of victoria blue and crystal violet

Jnyanashree Darabdhara, Berileena Hazarika, and Mohammed Ahmaruzzaman*

Department of Chemistry, National Institute of Technology Silchar-788010, Assam, India

*Corresponding author: Mohammed Ahmaruzzaman (e-mail: mazaman@che.nits.ac.in)

Abstract

The rising concerns regarding the discharge of waste effluents and their side effects in our environment has ignited the minds of different researchers for finding feasible, economic and practical ways to mitigate the ongoing alarming issue. Several harmful organic dyes, pharmaceuticals and nitro-aromatic compounds etc constitute the key harmful toxic contributors often found in the industrial wastes. This manuscript proposes the compositing of novel cauliflower leaves waste derived biochar (CF) with porous zinc-based metal organic framework (ZIF-8). The study of the crystalline planes, surface morphology, composition of different elements and optical features of the CF-ZIF-8 composite was examined through different analytical characterization methods including PXRD, TEM, FE-SEM, EDS, XPS, UV-DRS and PL analysis. The influence of the synergistic beneficial aspects of both the materials helped to boost the photocatalytic degradation performance of the CF-ZIF-8 catalyst with 92 ± 1.57% removal of victoria blue (VB) and 89 ± 1.21% removal of craystal violet (CV) and their degradation obeyed the first-order kinetics. The catalyst exerted a

maximum degradation performance at an optimized catalyst dosage of 18 mg, starting dye concentration of 30 ppm and pH 10. Under optimized conditions, the degradation rate constant for decomposition of VB and CV were 0.0474 min^{-1} and 0.0454 min^{-1} respectively. Moreover, from the scavenger analysis and PL investigations it was confirmed that the ·OH and $·O_2^-$ radicals were the key contributors for the photocatalytic breakdown of both the organic pollutant molecules. The CF-ZIF-8 catalyst also showed good sustainability as there was very little decline of the degradation efficiency until the fourth catalytic run and the intact of the crystalline structure revealed by the PXRD analysis with no appreciable changes in the PXRD pattern of the recycled catalyst.

Keywords: Cauliflower, Biochar, Photocatalytic Degradation, Metal Organic Frameworks.

1. Introduction

The accelerated growth in population, industrial progress and abrupt change in climate have severely compromised with the quality of water intensifying the global crisis for the need of fresh water. In lite of this, diverse entities that either consume or contaminate fresh water are the key contributors to the ongoing depletion in fresh water reserves[1]. Notably, the widely used dyes such as methyl orange (MO), methyl red (MR), rhodamine blue (RB), congo red (CR), crystal violet (CV), victoria blue (VB), methylene blue (MB) and Disperse Violet 26 are the key contributors to industrial water pollution that is released from multiple industries including the leather, textile, paper and pulp, paint and cosmetic industries etc[2-3]. The unregulated release of unprocessed dye contaminated wastewater into our

natural water reserviors negatively affects the photosynthesis mechanism in aquatic environment[5-7]. Existence of dyes in the environment can contribute to varying ranges of toxicity in human well-being such as cancer, kidney disorder, allergic responses, genetic mutations, and skin issues[8]. Therefore the improper dumping of dye containing effluents into our surrounding water reserviors adversely hampers quality of water, aquatic ecosysytem and public health.

Consequently, many researchers have directed their efforts towards the treatment of wastewater containing harmful dyes through different approaches. Many of such approches include filtration, advanced oxidation process, electrocoagulation, adsorption, sludge activation process, membrane bioreactors, ion-exchange, photocatalysis, and coagulation processes etc[9-10]. The process of breaking down of large pollutant molecules through the process of photodegradation has been adopted notably by different researchers for eliminating harmful organics present in industrial waste effulents in the last several years[11-12]. The mechanism of photocatalytic breakdown of organic molecules is based on heterogeneous catalysis wherein uses a semiconductor catalyst that harness the light from an illuminating source inorder to breakdown a range of environmental contaminants including those in aqueous and atmospheric systems. In contrast to the conventional water treatement techniques, the photocatalytic degradation process stands out as an advantageous alternative. As an example, an active photocatalyst may take just a few hours to fully degrade the organic molecules at ambient conditions. Furthermore, this process allows the complete breakdown of organic

compounds into less hazardous substances such as CO_2 and water, avoiding the creation of secondary toxic by products[13-16]. Ever since the report by Fujishima and Honda published in 1972, which demostrated that single crystals of TiO_2 can drive the splliting of water to generate hydrogen, rapid progression has been made in the field of photocatalysis[17]. The last many years has witnessed the significant intervention of photocatalytic oxidation process as an integral technique in water remediation processes. Since than several semiconductor photocatalytic materials have been addressed for the removal of water borne contaminants. In this context, some of the widely investigated photocatalyst are TiO_2[18], MoS_2[19], g-C_3N_4[20], CdS[21] and ZnO[22] etc. Nervertheless, despite their effective applications these catalyst showed evident challenges for large scale practical applications. Previous researchers has highlighted the key factors that contributes to the limited application of these materials. The rapid photoinduced electron-hole recombination results in weak photocatalytic decomposition of the organic substances, restricted use of the solar energy resulting from the narrow light absorption range, and insufficient active sites on the surface of the photocatalyst[23]. During the early nineties, a renowned scientist Yaghi pioneered the idea of Metal Organic Frameworks (MOFs) after the first successful development of MOF-5 comprising of a framework structure composed of organic linkers and metal centers[24]. Subsequently, this new type of material has become a prominent topic of extensive investigation. The metal organic frameworks are a type of porous structures characterized wih internal pores created by linking metal ion nodes or their clusters with different organic ligands that constitute the structural backbone of the

material[25]. With the growing extensive scientific investigations on MOFs, these materials have revealed their versatile applicability in a range of fields including chemical industries, energy storage, catalytic reactions, drug carriers, gas storage, luminescence and adsorption engineering[26-28].

With the recent progress of MOFs as photocatalytic materials, they display the following benefits over the conventional photocatalytic materials: their highly porous nature and the open structural framework promotes the easy transfer of pollutant molecules towards the active sites present on the catalyst surface[29]. Their remarkably large specific surface area and tunable porosity makes them ideal candidates for compositing with other active components. Finally, the incorporation of different functional groups enables the tailoring of spectral response range of MOFs[30]. Consequently driven by these characteristic advantages, the MOFs has gained much prominence in the area of photocatalysis, particularly for the catalytic breakdown of organic contaminants[31]. Zeolitic Imidazolate Frameworks (ZIFs), a sub-group of MOFs comprises of the same structural framework as other MOFs. They are formed by the coordination of metal ions such as Zn^{2+} or Co^{2+} with imidazole or their derivatives as the organic ligand constituting the framework structure through chemical bonds[32-33]. The ZIFs are the emerging class of substances with porous structures that harness the benefits of both zeolites and MOFs characteristics[34-37]. The ZIFs are often observed as promising porous materials for numerous applications due to the combination of several factors such as controllability of pores, structural diversity, thermal durability, tunability of pores and large surface area[38]. Besides the several beneficial characteristics, the ZIFs also displays some

disbenefits which restrains their application. For instance, the ZIF-8 nanoparticles has a tendency to undergo agglomeration in aqueous phase that enlarges their particle size, hampers their rate of charge transfer and also reduces their available interfacial area that ultimately impairs their adsorption efficiency[39]. The wide optical band structure of ZIF-8 limits the application of the material only in Ultra-Violet region[40]. Over the recent years there has been numerous investigations on the use of ZIFs in the area of photocatalysis. Various efforts have been directed for synergizing ZIFs with other materials to achieve highly improved photocatalytic efficiency[41]. In constrast to the corresponding individual component photocatalyst, the carefully engineered composite material photocatalyst harness the corresponding advantages of both the individual components while counterbalancing the limitattions of individual components leading to enhanced photocatalytic efficiency[42]. Utilization of materials based on solid wastes have recently been identified as promising substances for the treatement of waste effluents allowing to serve dual purpose addressing the issue of both solid waste management and waste water treatement[43]. Recently many studies have highlighted different thermochemical processes widely used for the conversion of solid waste into biochar. Biochar is considered as an eco-friendly and viable material due to the presence of diverse functional groups, higly porous surface, high surface area, strong cation exchange capacity and longer stability[44-45]. Biochar is generated through the carbonization of biomass in presence of minimal oxygen supply. C, O, N and S constitute the key components of biochar [46]. Owing to the pronounced charge transport capability and excellent electrical and thermal

conductivity, there has been extensive use of carbon based materials such as the carbon nanotubes and reduced graphene oxide in order to boost the photocatalytic performance[47-50]. Their strong ability to adsorb harmful organic molecules, numerous surface functional groups and their strong electrical conductivity make them an outstanding material for improved photocatalytic efficiency[51]. In this manuscript we highlight the fabrication of biochar-ZIF-8 material through compositing cauliflower derived biochar with ZIF-8. Very limited literatures have discussed the application of ZIF-8 with biochar for utilization of naturally available solar light for photocatalytic breakdown of environmental pollutants. Although there has been reports of composite formation of ZIF-8 with biochar originated from different sources, however there has been no reports till date discussing the formation of ZIF-8-biochar composite derived from waste cauliflower leaves for the removal of specially CV and VB. Different analytical methods including Fourier transform infrared spectroscopy (FTIR), Powder X-ray Diffraction (PXRD), Transmission electron microscopy (TEM), Field Emission-Scanning electron microscopy (FE-SEM), X-ray photoelecton spectroscopy (XPS), Ultra-Violet Reflectance Spectroscooy (UV-DRS) and Photoluminescence (PL) analysis were used for the confirmation of the composite formation. The environmental usefulness of the composite was studied by the photocatalytic degradation of two commonly found harmful organic dye molecules in the environment. The several factors such as the variation of the catalyst amount, starting concentration of the investigated contaminant solutions and pH that can possibly influence the photocatalytic process was also tested.

2. Experimental

2.1. Chemicals and Methods

The cauliflower leaves were purchased from a weekly market located near the vicinity of NIT Silchar. The other chemicals that were used in the synthesis of the CF-ZIF-8 composite included Zinc nitrate hexahydrate ($Zn(NO_3)_2.6H_2O$) and 2-methylimidazole (Hmim), both the chemicals were procured from Sigma Aldrich. The two dyes CV and VB used in the degradation studies were purchased from SRL, Private limited India. The sythesis procedure involved the usage of analytical grade chemicals and they were used as purchased. All the solutions used in the experiments were prepared ultrapure water provided by the Ultrapurification Unit- Milli pore Milli-Q system showing18.25 M resistivity.

2.2. Preparation of CF Biochar

For the synthesis of CF biochar, initially the Cauliflower leaves were first gathered from the vicinity of NIT silchar and underwent repetitive washes thoroughly using distilled water. The cauliflower leaves were than subsequently left for drying inside a hot air oven with the temperature set at 80ºC for 48 hours inorder to eliminate remaining volatile impurities. The dried cauliflower leaves were subsequently pulverised finely. The material was latter on subjected for thermal treatement at 300ºC inside a muffle furnace for 120 minutes. The resulting biochar was crushed into fine particles with the help of a mortar and passed through a 0.25 mm mechanical sieve inorder to separate small particle[52].

2.3. Preparation of CF-ZIF-8 composite

A 25 ml methanolic solution of $Zn(NO_3)_2.6H_2O$ (2.5 mmol) was gradually poured into another methanolic solution of Hmim (20 mmol) kept in a magnetic stirrer. The solution was left for stirring till 15 minutes until the addition of 400 mg of the synthesized CF-biochar. The solution was left for stirring till 12 hours. The solid product was separated from the solution by centrifuging at 1600 rpm followed by washing the product multiple times with methanol. The material was dried inside a hot air over for 14 hours at 80º C. It was than thermally treated inside a muffle furnace with the temperature set at 300º C with a heating ramp rate of 5º C per minute for 210 minutes. The fine black couloured material was obtained after heat treatment was name as CF-ZIF-8[53]

2.4. Exploration of Photocatalytic Efficiency

Inorder to access the photocatalytic performance of the as prepared CF-ZIF-8 composite, the photocatalytic breakdown of two typical organic dye molecule i.e. VB and CV was tracked under the exposure of natural sunlight. Before initiating the photocatalytic degradation study, a 40 minutes of continuous stirring period in the dark was carried on for investigating the dye adsorption study. Just a minimal amount of the dye was adsorbed on the surface of CF-ZIF-8 composite, before exposing the raction mixture under sunlight. All experiments related to degradation were carried out on a suuny day in September month from 10:30 am to 3:30 pm. The intensity of the solar irradiance ranged from 4.47-4.71 Wm^{-2} recorded by a solar power meter TENMARS TM 207 and the reocorded temperature was approximetly ~34ºC. For the photocatalytic degradation process, different weight 12-18 mg (0.34-0.51 g/L) of the CF-ZIF-8 catalyst were added to 35 ml of each CV

and VB dye solutions with there concentration ranging from 30 mg/L to 60 mg/L. Inorder to evaluate the progress of photocatalytic degradation process, 2 ml of the monitored solution was extracted at a fixed interval of time. Centrifugation process was applied for isolation of the catalyst dispersed in the dye solutions. The progession of photocatalytic removal of both the dyes was assessed through a UV-Visible spectrophotometer, which showed a steady decrease in the characteristic absorption peak at ~579 nm (CV) and 613 nm (VB). The equation (1) below was used to compute the degradation efficiency (%) of the investigated CF-ZIF-8 photocatalyst.

$$\text{Degradation Efficiency (\%)} = \frac{C_o - C_t}{C_o} \times 100 \quad (1)$$

C_o in 'mg/L' refers to the original concentration of the dye used for analysis at t=0 minute

C_t in 'mg/L' refers to the dye concentration at "t" time in minute

2.5. Characterization of the material

The crystallographic features of the as newly synthesized composite was carried out via PXRD analysis with Bruker D8 Advance X ray diffractometer illuminating Cu-Kα radiation with 1.5418 Å measured wavelength, 2ɵ ranring from 5 to 70º. The analysis of the various functional groups constituting the composite was studied through FTIR analysis recorded in Bruker Hyperion 3000 FTIR Spectrometer in the range 400-4000 cm^{-1}. The elemental characterization of the CF-ZIF-8 composite was studied through XPS analysis with PHI 5000 versaprobe II FEI Inc. The d spacing value of the lattice fringes obtained from HR-TEM and SAED patterns were recorded in JEOL, model name JEM 2100F operating at 200kV. SEM analysis was

performed to study the morphology of the composite surface investigated with Gemini 500 FE−SEM instrument. The estimated band gap of the composite furnished by the UV-DRS analysis was obtained in Cary 5000 UV–vis–NIR, Agilent Inc. spectrophotometer. The photoluminescence analysis was recorded in Varian Cary eclipse fluorescence spectrophotometer. The absorption studies of the dye solutions investigated in the photocatalytic degradation analysis were recorded with Genesys 10S UV visible spectrophotometer within the wavelength range 200-800 nm.

3. Results and Discussion

3.1. FT-IR

FTIR spectroscopy was employed in order to make analysis of the several functional groups constituting the CF-ZIF-8 composite. The FTIR spectra as shown in **Fig 1(a)** highlights the different surface functional groups composing the CF biochar sample. Biochars in most cases are primarily derived from biomass feedstock that are rich in cellulose. Cellulose are polymers comprising of abundant hydroxyl groups, they retain some of these group in the sample even post pyrolysis, hence the peak appeared at 3334 cm^{-1} can be assigned to the stretching vibrations of the O-H groups[54]. The 1420 cm^{-1} peak indicate the C-H bending vibrations of the corresponding CH_2 group. The infrared peak at 1030 cm^{-1} indicate the C-O stretching vibrations of 2º alcohols. The occurrence of the peaks at 887-668 cm^{-1} signifies the bending vibrations of aromatic C-H[55]. After compositing with ZIF-8, all the peaks occuring due to the CF biochar and ZIF-8 could be found in the IR spectra of the CF-ZIF-8 composite. The IR spectrum of the CF-ZIF-8 composite shows new characteristic infrared peaks at 3138, 2923,

1586 and 1143 cm^{-1} apprearing due to the different functional groups of the imidazole linker of the ZIF-8. C-H stretching bands which are characteristic to the Hmim ligand could be found at 3138 cm^{-1}(aromatic) and 2923 cm^{-1}(aliphatic) in the IR spectrum of CF-ZIF-8. The absorption peak at 1586 cm^{-1} suggest the stretching motion of the C=N bond of the imidazole linker. The band due to the characteristic C-N vibration appeared at 1143 cm^{-1}. The spectral bands at 754 and 689 cm^{-1} are attributed to the out of-plane bending modes of the imidazole ligand[56], **Fig 1(b)**.

3.2. XRD

The PXRD analysis of the CF biochar revealed a broad diffraction peak at 22.2º, associated with the (002) crystal plane and signifies the amorphous carbon nature, **Fig 2(a)**[57]. Upon integrating the ZIF-8 into the CF biochar matrix, the CF-ZIF-8 composite revealed characteristic peaks at different 2ɵ angles of 7.28º, 10.38º, 12.75º, 14.71º, 16.41º, 18.08º, 22.26º, 24.63º, 26.83º and 29.73º etc aligning with the (110), (200), (211), (220), (310), (222), (411), (332), (431) and (440), **Fig 2(b)**[58]. These observed peaks validate the effective impregnation of the particles of the Zn based MOF, ZIF-8 into the surface of CF biochar matrix, leading to favourable formation of the CF-ZIF-8 composite.

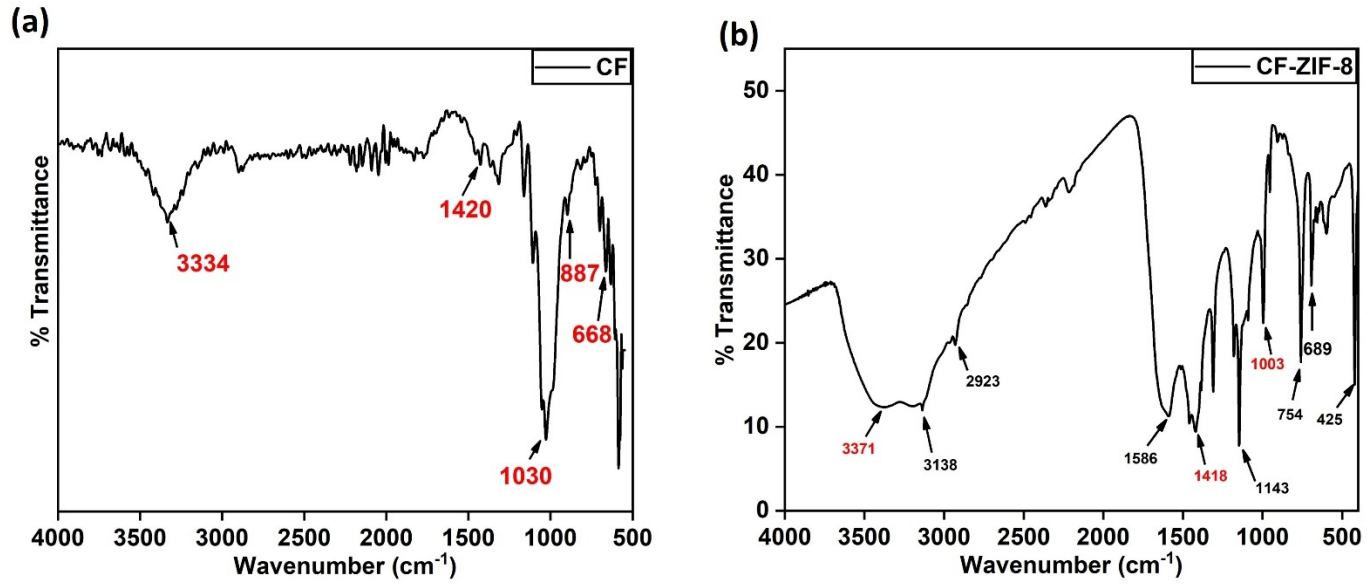

Fig 1: FTIR spectra of (a) Cauliflower leaves biochar (b) CF-ZIF-8 composite

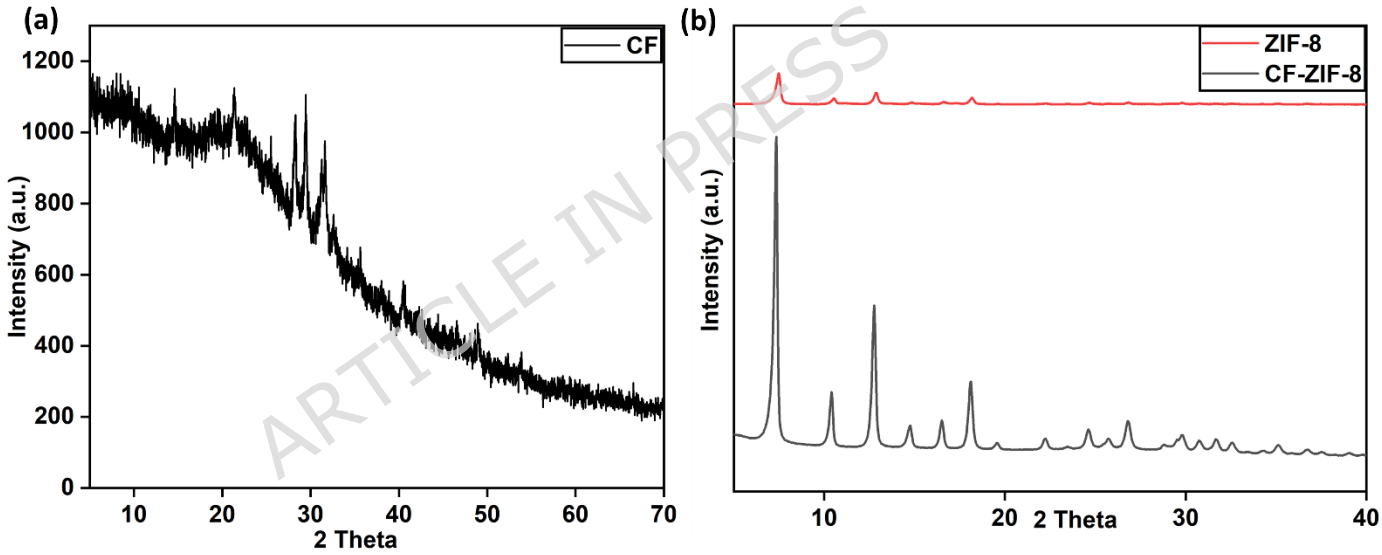

Fig 2: X-ray Diffraction analysis pattern of (a) Cauliflower leaves Biochar (b) ZIF-8 alone and CF-ZIF-8

3.3. UV-DRS

The performance of the catalyst is largely governed by its capacity for absorption of light and the value of the band gap structure. As can be seen from **Fig 3(a)** both bare ZIF-8 and CF-ZIF-8 shows appreciable absorption properties in the ultra violet (UV) region. Bare ZIF-8 displays an absorption

edge at 248 nm and it shows very negligible absorption of visible light in the visible range[59]. However, after conjugating it with CF biochar matrix, the CF-ZIF-8 shows tremendous improvement in the absorption capacity in the visible range which indicate the ability of the catalyst to absorb both UV and visible light for photocatalytic applications[60]. In addition, the optical energy band gap of CF-ZIF-8 was estimated with the help of Wood and Tauc Plot, as represented by the equation (2) below:

$$\alpha h\upsilon = A(h\upsilon - Eg)^{n} \quad (2)$$

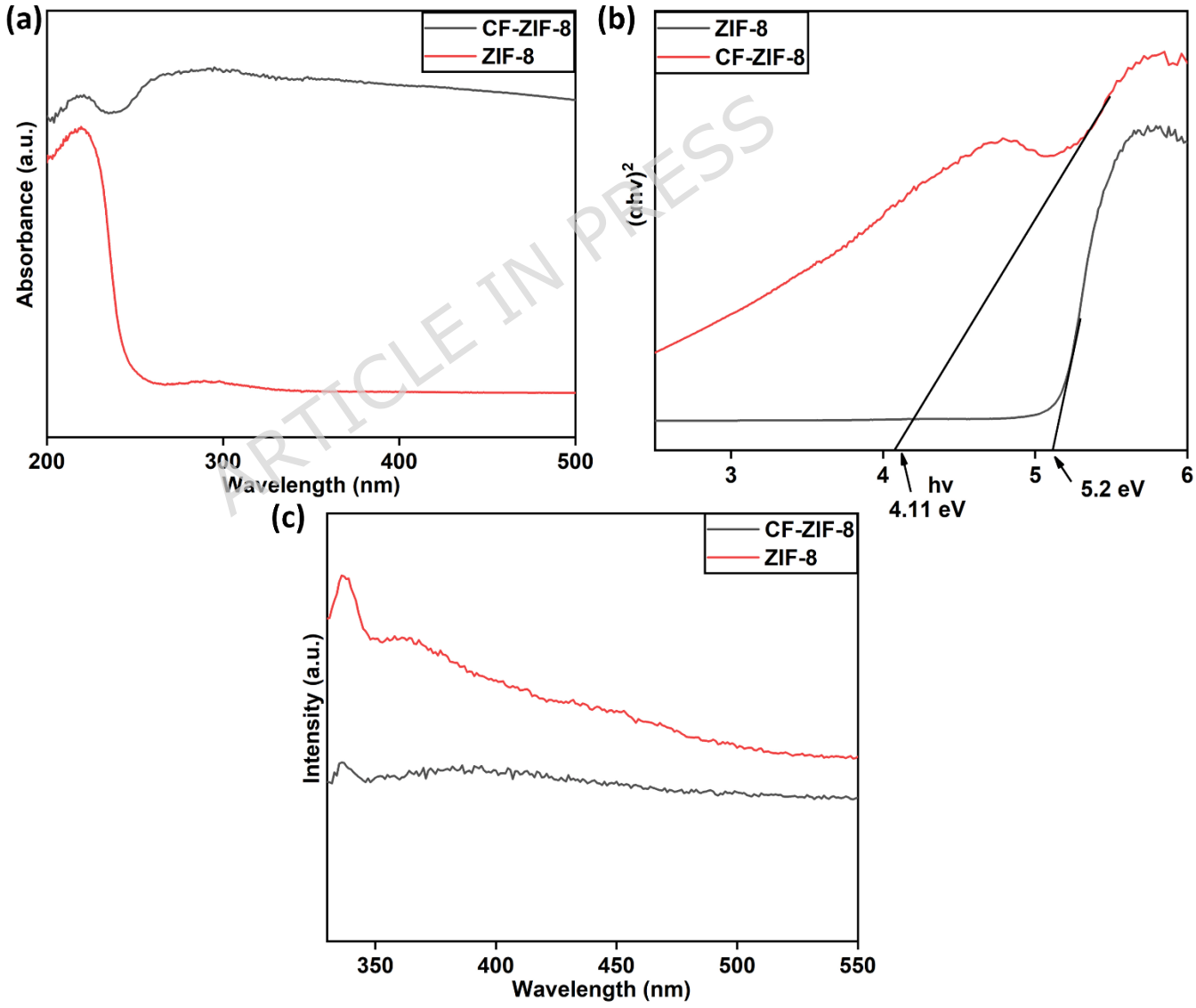

Fig 3: UV-Visible Diffuse Reflectance Spectroscopy of (a) ZIF-8 alone and CF-ZIF-8 composite; (b) Calculated energy of optical band gap from Tauc's plot for ZIF-8 alone and CF-ZIF-8; (c) Comparison of intensity of the PL spectrum of ZIF-8 alone and CF-ZIF-8 composite

In this context, the term hυ refers to the photon energy, α refers to the absorption coefficient and E_g signifies the optical energy band gap. In order to determine the band gap, $(\alpha h\upsilon)^2$ vs hυ plot towards the point where the absorption become negligible in the abscissa was extended. The energy of the band gap for ZIF-8 and CF-ZIF-8 was found to be 5.2 and 4.1 eV, **Fig 3(b)**. Thus, combining CF-biochar with ZIF-8 boosts the ability of the material for absorption of light and also narrow down the band gap energy. This outcome suggests that incorporation of ZIF-8 with the CF-biochar matrix improves the photocatalytic performance of the ZIF-8 alone. The CF-Biochar on the other hand, also promotes the separation of charge carriers i.e. e^- (electrons) and h^+(holes), which is a key factor for the superior photocatalytic performance of the CF-ZIF-8 catalyst. To validate this finding, photoluminescence (PL) measurements were conducted (λ_{ex}=300 nm) for evaluating the effective separation of the photoinduced electron and hole pairs in the CF-ZIF-8 composite. In general, lower photoluminescence intensity is usually associated with lower recombination rate of photoexcited e^- and h^+[61]. It is noteworthy that the composite CF-ZIF-8 shows lower PL intensity than bare ZIF-8 which reflects the superior ability of CF-ZIF-8 to separate photogenerated e^- and h^+ than corresponding bare ZIF-8, **Fig 3(c)**. The CF-biochar is thus believed to serve as a suitable

electron acceptor, thereby reducing the ability of the recombination of photogenerated e^- and h^+ during exposure to light.

3.4. XPS Analysis

As illustrated by **Fig 4**, the elemental chemical states in CF-ZIF-8 composite were characterized with the help of XPS analysis. The survey spectra **Fig 4(a)**, showed the major elements present in CF-ZIF-8 composite were C, N, O and Zn. Absence of additional characteristic peaks confirms only the presence of expected elements in the CF-ZIF-8 composite with no further signs of any kind of contamination. The deconvoluted XPS spectra of Zn 2P features two characteristic signals located at 1022.1 and 1045.5 eV which are characteristic of Zn $2P_{3/2}$ and Zn $2P_{1/2}$, **Fig 4(b)**[62]. Carbon and its related functional groups were verified by deconvoluting the C1s XPS spectrum from the main peak at 285. 1 eV into multiple peaks at 284.8, 286.5 and 288.9 eV confirming the presence of carbon related groups C-C, C-N and C=O in the CF-ZIF-8 composite, **Fig 4(c)**[63]. Two distinct peak features in the N1s spectrum of CF-ZIF-8 at 389.9 and 400.5 eV assigned to the different nitrogen environments of the imidazole linker. The above findings clearly demonstrate the successful formation of the CF-ZIF-8 composite, **Fig 4(d)**.

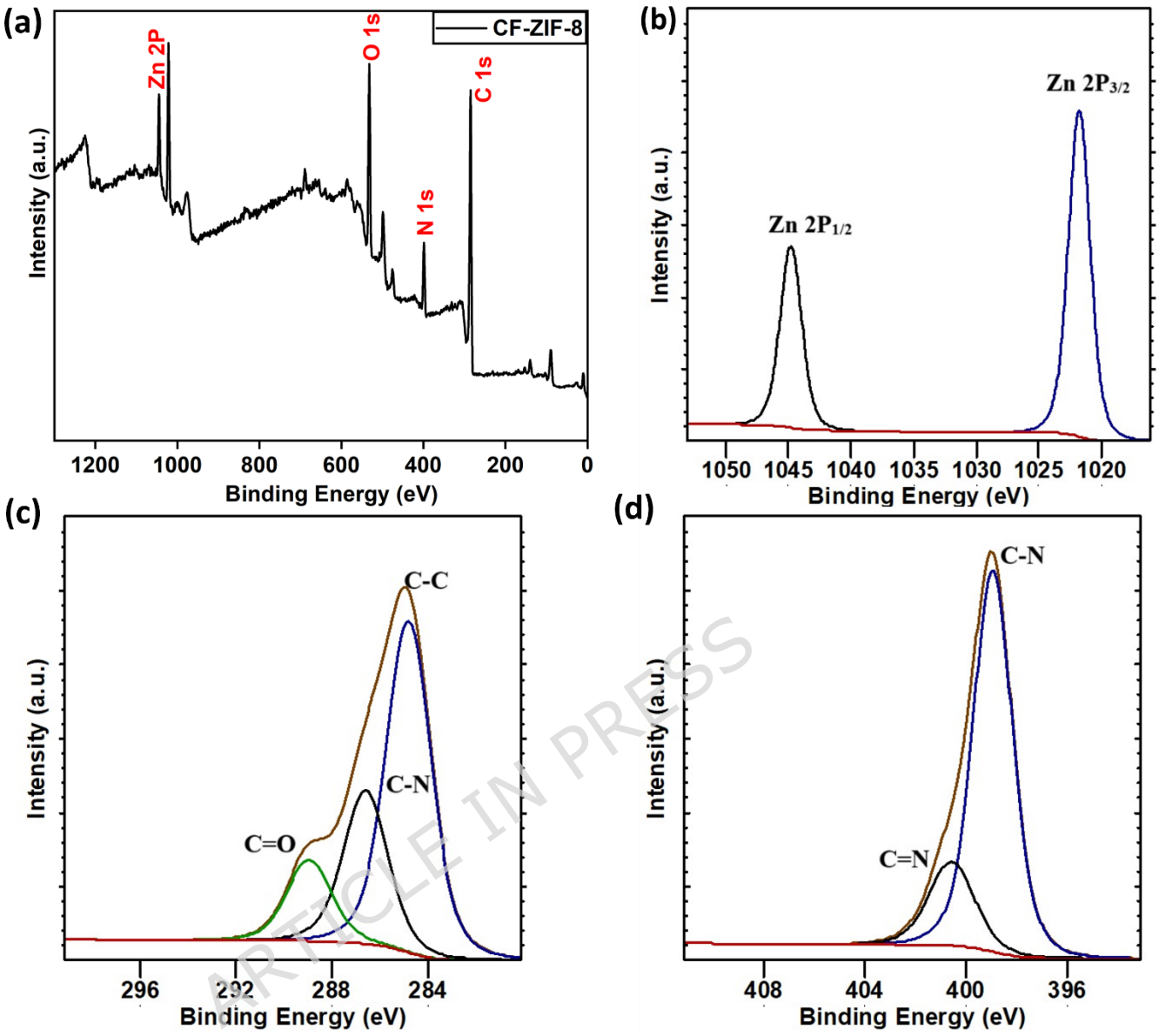

Fig 4: (a) Survey spectrum of the XPS elemental analysis of CF-ZIF-8 composite; (b) High-Resolution XPS spectra of the constituting elements (b) Zn 2p (c) C 1s and (d) N 1s.

3.5. FESEM and TEM analyses

FESEM and TEM analyses were conducted to examine the morphology of the surface of ZIF-8 and CF-ZIF-8 composite. **Fig 5(a-b)** reveals the surface characteristic and shape of bare ZIF-8 paticles, **Fig 5 (c)** demonstrates the

surface morphology of CF-ZIF-8 composite. It is evident from the image that the ZIF-8 particles are succesfuly developed on the CF biochar surface, ensuring strong integration of both the materials. The ZIF-8 particles in CF-ZIF-8 **Fig 5(d)**, resembled the same characteristic morphology as that of bare ZIF-8, **Fig 5(b)**. HR-TEM micrograph of CF-ZIF-8 composite is shown in **Fig 5(e)**. From the lattice fringes found in the HR-TEM image of CF-ZIF-8, the value of the d spacing between them was measured as 0.41 nm, matching with the (321) crystal plane of ZIF-8. The SAED pattern in **Fig 5(f)**, demonstrates the d-spacing between the lattices which closely is associated with the (411) plane of ZIF-8. To gain further insights into the composition of the CF-ZIF-8 composite, energy dispersion X-ray spectroscopy (EDX) was conducted, **Fig 5(g)**. The results shows peaks corresponding to the distribution of elements such as Zn, N, O and C on the surface of the materials thus reflecting that the ZIF-8 particles were uniformly distributed, covering the surface of CF-biochar. The weight percentage and atomic percentage of the several elements forming the CF-ZIF-8 composite are also revealed in the **Fig 5(g)**. The microstructural analysis results thus indicate the development of ZIF-8 particles on the surface of the CF-biochar.

4. Assessment of Photocatalytic Efficiency of CF-ZIF-8

4.1. Influence of catalyst concentration

Optimizing the catalyst dosage is crucial to avoid the unnecessary over consumption of the photocatalyst and also to minimize the operational cost. The photocatalytic degradation behaviour of CV and VB (30 mg/L) were conducted by altering the concentration of the photocatalyst from 12-18 mg

(0.34-0.51 g/L) to 35 ml of both the targeted solutions. The study included 50 minutes of sunlight exposure to each of the solutions. **Fig 6(a)** and **Fig 6(c)** describe the rising trend in the photocatalytic degradation efficiency of CF-ZIF-8 with increasing the catalyst concentration from 12-18 mg (0.34-0.51 g/L) at first, while the rate of the reaction diminished with the addition of the catalyst loading beyond the optimized level.

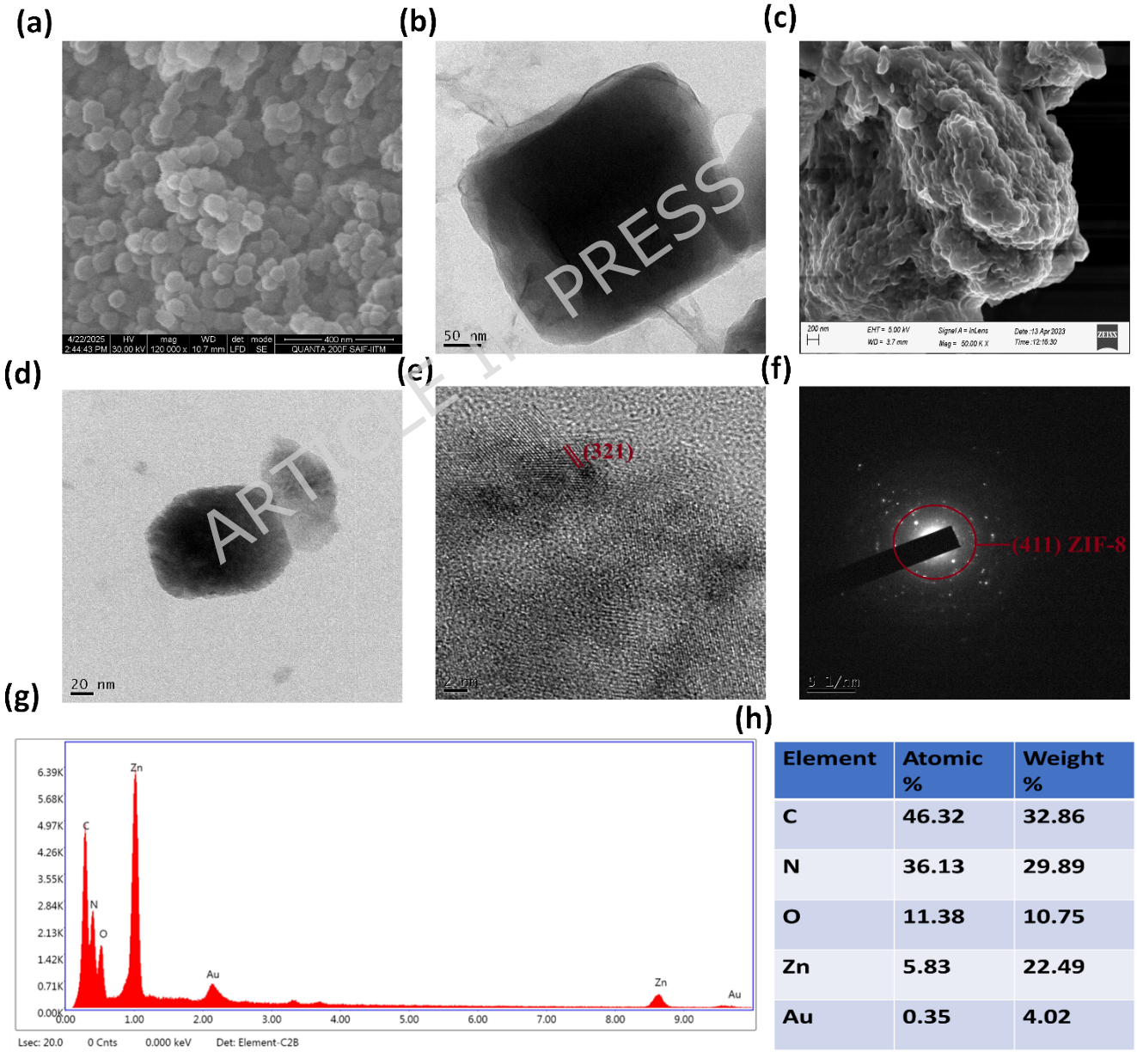

Element	Atomic %	Weight %
C	46.32	32.86
N	36.13	29.89
O	11.38	10.75
Zn	5.83	22.49
Au	0.35	4.02

Fig 5: (a) FESEM of ZIF-8; (b)TEM image of ZIF-8; (c) FESEM image of CF-ZIF-8; (d) TEM image of CF-ZIF-8; (e) High Resolution-TEM image of CF-ZIF-8; (f) SAED pattern of CF-ZIF-8; (g) EDX of CF-ZIF-8 (h) Percentage of different elements constituting CF-ZIF-8 from EDX analysis

The greater photodegradation efficiency corresponding to the high photocatalyst dosage is the consequence of the abundant availability of the active sites and elevated formation of ·OH (hydroxyl) radical. 18 mg (0.51 g/L) of the photocatalyst resulted 92.9 ± 2.10% and 89 ± 1.22% degradation of VB and CV with a rate constant of 0.0498 and 0.0440 min^{-1}, **Fig 6(b)** and **Fig 6(d)**. However, increasing the catalyst dosage beyond 20 mg resulted with declining of the photocatalytic degradation efficiency. This observed drop in the degradation efficiency after the overdose of the photocatalyst can be because of the surplus generation of ·OH radicals which then deactivated through mutual quenching process[64]. Also, surplus amount of the photocatalyst results in densely concentrated or opaque solution which attenuates with the penetration of photons reaching the photocatalyst surface.

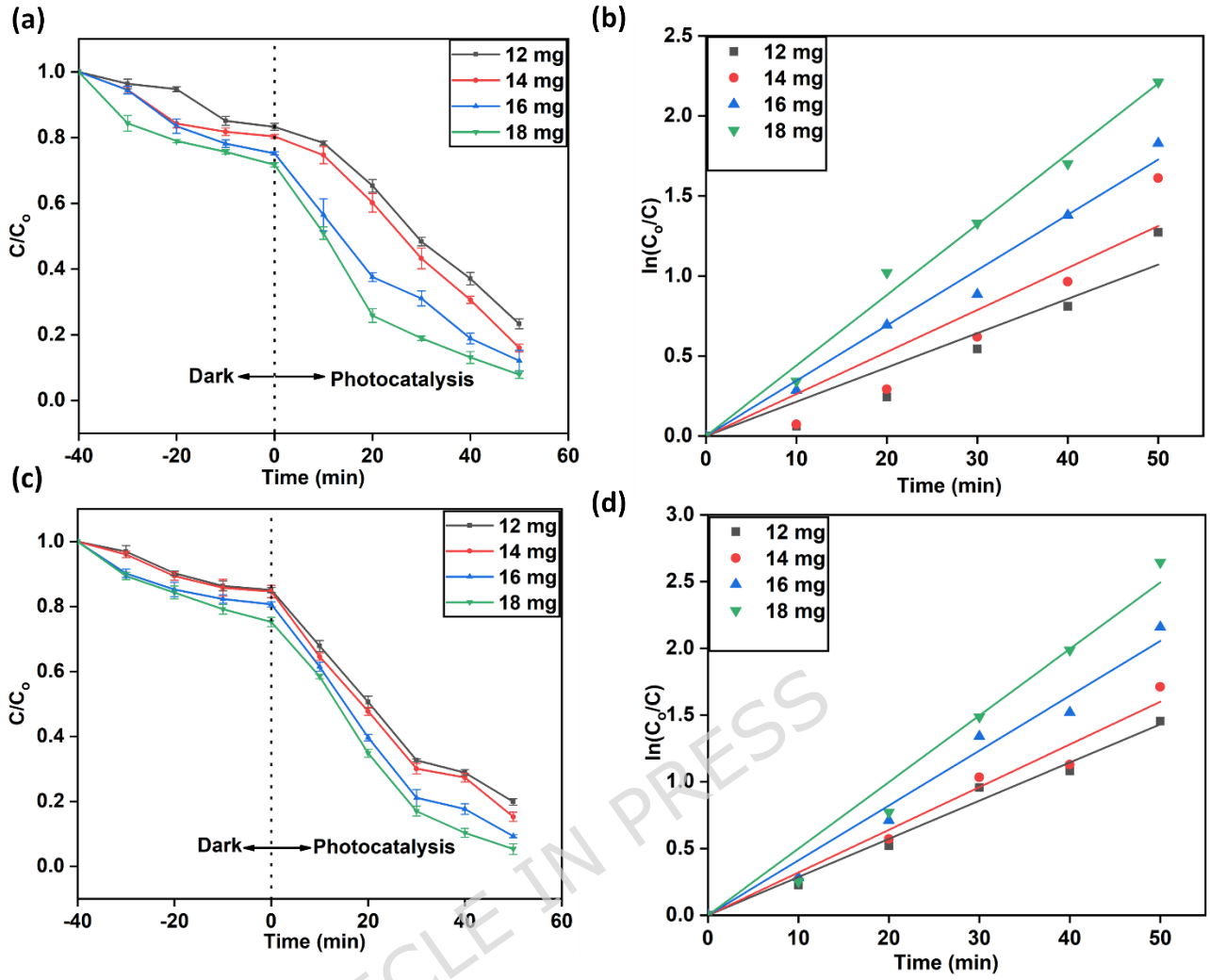

Fig 6: (a) Photocatalytic breakdown profile, C/C_o vs time plot of CV at different catalyst dosage; (b) study of the corresponding degradation kinetics, $\ln(C_o/C)$ vs time plot of CV at different catalyst dosage; (c) Photocatalytic degradation profile, C/C_o vs time plot of VB in presence of different catalyst dosage; (d) study of the corresponding degradation kinetics, $\ln(C_o/C)$ vs time plot of VB at different catalyst dosage

4.2. Influence of the starting concentration of CV and VB

The starting contaminant concentration critically influences the overall photodegradation efficiency of the photocatalyst. Therefore, it is crucial to

identify the optimizable limit of contaminant concentration that can be degraded effectively by the optimized concentration level of the photocatalyst. **Fig 7(a)** and **Fig 7(c)** clearly display the impact of varying starting concentration of CV and VB on the photocatalytic efficiency of CF-ZIF-8 under optimized reaction conditions of photocatalyst amount 18 mg (0.51 g/L). It is evident from **Fig 7(b)** and **Fig 7(d)** that the highest breakdown of CV (89 ± 2.06%) and VB (92 ± 2.32%) was achieved at 30 mg/L concentration level. And the calculated rate constant for the pseudo first order photocatalytic breakdown of CV and VB was found to be 0.03651 and 0.04138 min^{-1}. For higher concentrated solutions of the contaminants, a drop in the degradation activity of the catalyst was found which can be possibly linked to the obstruction of the photons path, and constricted path length of the photons for highly dense dye solutions[65]. Moreover, an elevated contaminant concentration would necessitate a surplus quantity of the photocatalyst which may increase the solution's turbidity and thus inhibits the degradation of the targeted contaminants[66]. Increased concentration of the targeted contaminants may result in the saturation of the catalyst's active sites by contaminant molecules pushing away the surface bound oxygen molecules and hydroxide ions[67]. Consequently, this effect suppresses the formation of different reactive oxygen species including the $^{\cdot}O_2^-$ (superoxide) and $^{\cdot}OH$ radicals which cause the photocatalytic breakdown of the targeted contaminants[68]. This process negatively impacts the photocatalytic performance of the catalyst.

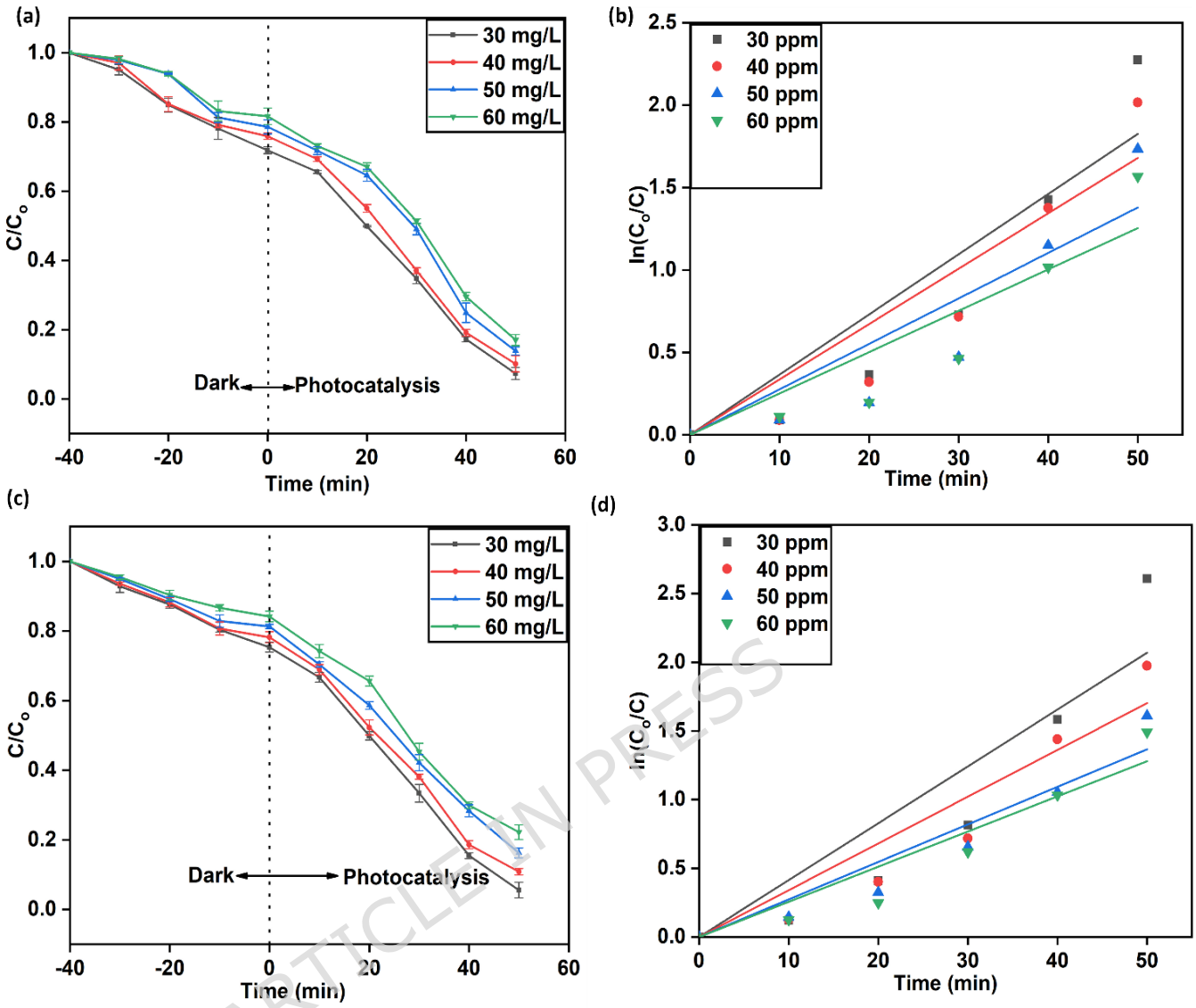

Fig 7: (a) Study of the degradation efficiency of CF-ZIF-8 catalyst, C/C_o vs time plot at different starting concentration of CV; (b) Study of the corresponding degradation kinetics, $\ln(C_o/C)$ vs time plot at different starting concentrations of CV; (c) Study of the degradation efficiency of CF-ZIF-8 catalyst, C/C_o vs time plot at different starting concentration of VB; (d) Study of the corresponding degradation kinetics, $\ln(C_o/C)$ vs time plot at different starting concentrations of VB.

4.3. pH optimization

To examine the role of pH in the photocatalytic breakdown of the targeted contaminants CV and VB, batch experiments were performed using 18 mg (0.51 g/L) of the fabricated CF-ZIF-8 photocatalyst at a starting contaminant concentration of 30 mg/L and the pH varying across 4-10. All the experiments were conducted under optimized parameters and illuminated under sunlight for 50 minutes. As it is evident from the **Fig 9(a)** and **Fig 9(c)** that the highest photocatalytic breakdown was seen at pH 10 for both VB (92 ± 1.71%) and CV (89 ± 1.21%) and the rate constant of degradation was calculated as 0.0394 and 0.0369 min^{-1}, Fig 9(b) and 9(d). The pronounced degradation of CV and VB under alkaline conditions can be ascribed to the high availability of hydroxide (OH^-) ions that promotes the ·OH radical production by interacting with the photogenerated h^+ according to the equation (3) below. The greater yield of ·OH radicals leads to pronounced discoloration of the dye solutions[69]. Additionally, the value of the zeta potential -28.2 mV as suggested from the DLS results at 7.5 pH level, **Fig 8**, indicates the occurrence of negatively charged catalyst surface at alkaline conditions. Therefore, the pronounced degradation of both the targeted dye contaminants under alkaline medium is also the result of the electrostatic interactions occurring between the negatively charged catalyst surface and the positive dye molecules[70]. In contrast, under acidic environment the accumulation of the surface of the catalyst with H^+ ions induces electrostatic repulsion with the cationic dye molecules thus suppressing their decolourisation by CF-ZIF-8 catalyst[71].

$$OH^- + h^+ \longrightarrow {}^{\cdot}OH \quad (3)$$

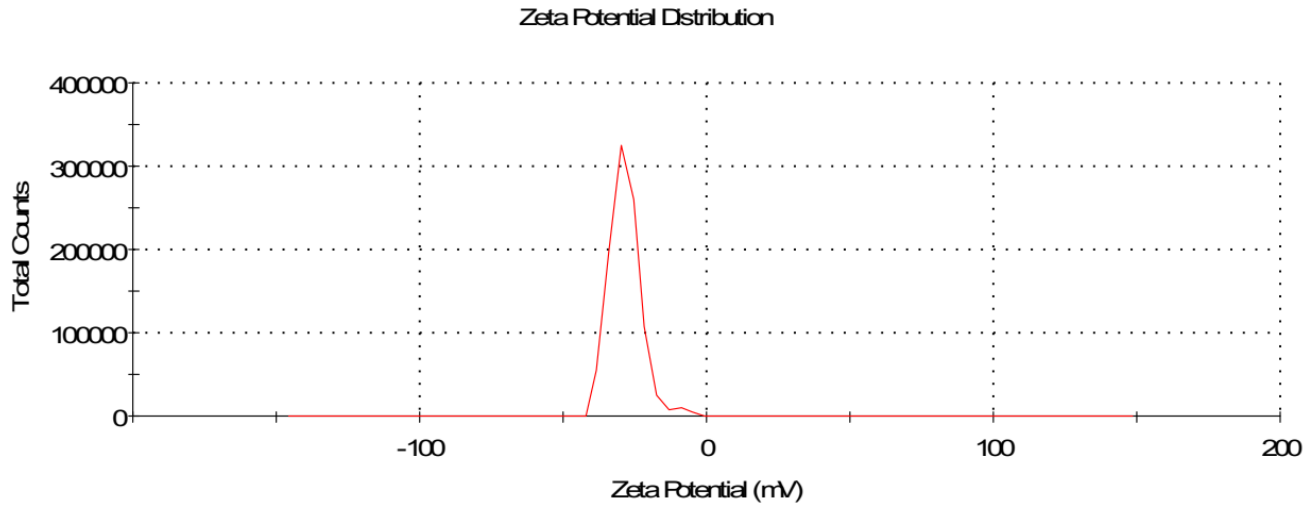

Fig 8: Plot of Zeta Potential of CF-ZIF-8

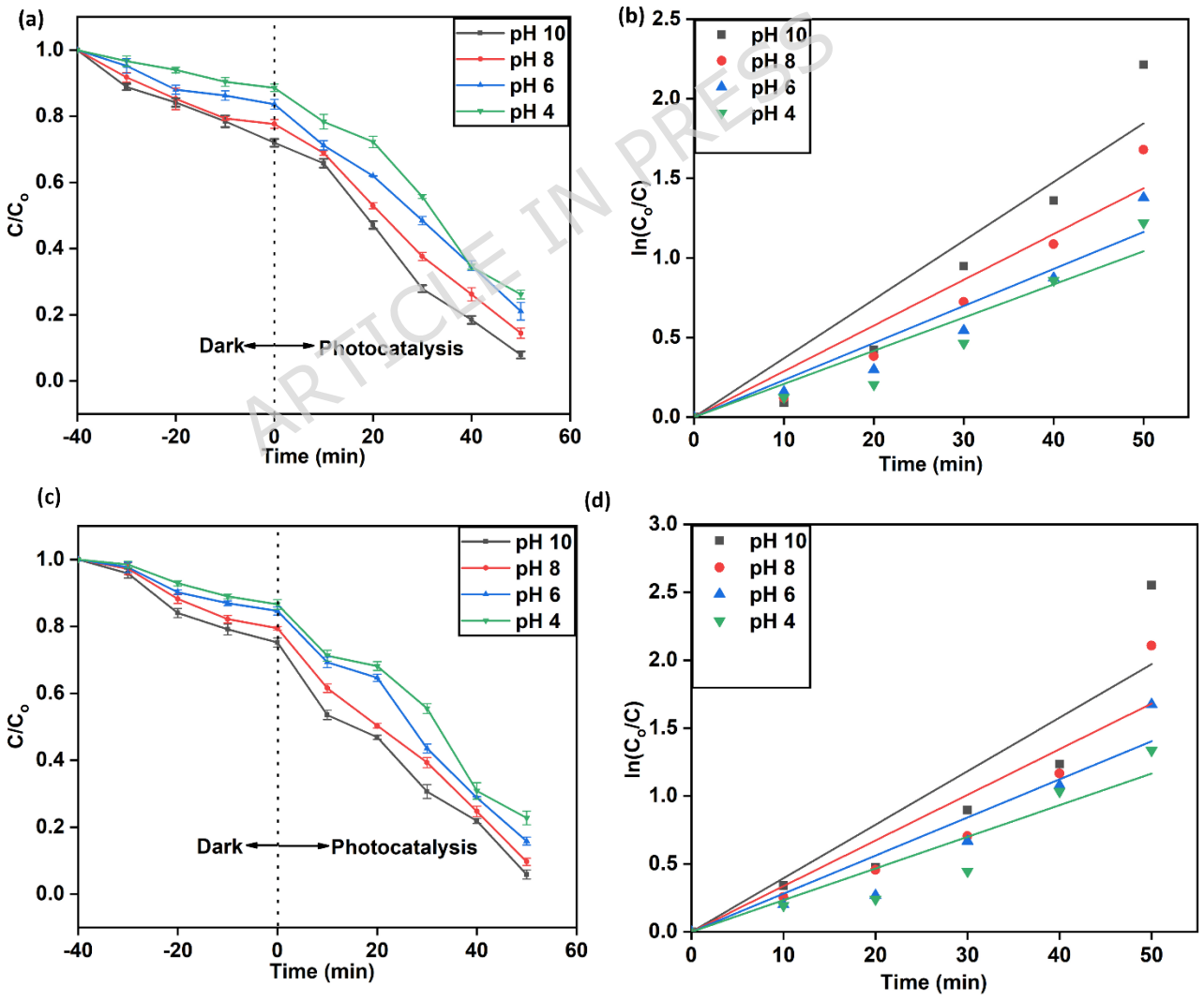

Fig 9: (a) Degradation efficiency of CF-ZIF-8 catalyst, C/C_o vs time plot for CV dye solutions at different pH; (b) Corresponding degradation kinetics, $\ln(C_o/C)$ vs time plot for the CV solutions at different pH; (c) Degradation efficiency of CF-ZIF-8, C/C_o vs time plot for VB dye solutions at different pH; (d) Corresponding degradation kinetics, $\ln(C_o/C)$ vs time plot for the VB solutions at different pH.

4.4. Overview of the photocatalytic degradation efficiency of CF-ZIF-8

To evaluate the synergistic influence of CF biochar and ZIF-8 contributing to the photocatalytic breakdown of CV and VB by using the synthesized CF-ZIF-8 catalyst was studied under optimized reaction conditions of catalyst dosage 18 mg (0.51 g/L), dye concentration 30 mg/L and pH 10 respectively. **Fig 10(a)** and **Fig 10(c)** presents the performance of the CF-ZIF-8 photocatalyst for decolorization of 35 ml solution of CV and VB under sunlight irradiation for a period of 50 minutes. The changes in intensity in the UV visible curve of CV and VB degradation clearly illustrates the efficient photocatalytic decolorization of both the contaminants in presence of sunlight exposure. Before subjecting the dye solutions under sunlight irradiation, the dark reactions were also investigated to evaluate the extent of adsorption of both the targeted contaminants by the CF-ZIF-8 catalyst. The CF-ZIF-8 showed very minimal adsorption capturing only small percentage of the contaminants CV (28 ± 1.69%) and VB (24 ± 0.99%). However, after 40 minutes of running in the dark there was no significant sign of adsorption in case of both the dye solutions. On the other hand, after

50 minutes of irradiation under sunlight the CF-ZIF-8 catalyst showed the maximum photocatalytic decolourization of VB (92 ± 1.57%) and CV (89 ± 1.21%). Table 1 enlists the several catalysts that have been recently reported for the photocatalytic breakdown of CV and VB. The photocatalytic breakdown of both the targeted contaminants by CF-ZIF-8 catalyst was compared under the same optimal reaction conditions but in presence of the pristine materials CF biochar and ZIF-8, **Fig 10(e)** and **10(f).** Only marginal photocatalytic decolorization of the targeted contaminants was seen in case of pristine ZIF-8 (33 ± 1.80% of CV and 29 ± 1.91% of VB) and CF biochar (14 ± 2.43%) CV and 10 ± 2.29% VB). Under the identical reaction parameters, the self-photodegradation of CV and VB was almost negligible without the presence of any photocatalyst. This boost in the efficiency of the photocatalytic degradation of the targeted contaminants can be attributed to multiple synergistic factors including the better separation of charge in the CF-ZIF-8 catalyst promoted due to the occurrence of the biochar phase, the occurrence of ample functional groups on the surface of the biochar that facilitates the better interaction between the catalyst surface and the contaminant molecules and strong light adsorption characteristics as evident from the UV-visible analysis[72].

4.5. Kinetic Study Analysis of Degradation of both the dyes via Photocatalysis Process

The kinetic study relating to the photocatalytic decolorization of both the contaminants (CV and VB) by CF-ZIF-8 catalyst was examined with the help of two kinetic reaction models namely the first order and second order equation (equations 4 and 5) presented below:

$$\ln \frac{C_o}{C} = kt \quad (4)$$

$$\frac{1}{C} - \frac{1}{C_o} = kt \quad (5)$$

C_o measured in mg/L refers to the dye concentration at time 't'=0 min. C measured in mg/L reflects the dye concentration at any moment of time "t" and k in min^{-1} states the kinetic rate constant of degradation of CV and VB under optimized conditions[73]. As referred by **Fig 10(b)** and **10(d)** the linear relationship between $\ln(C_o/C)$ and time for the photocatalytic decomposition of both the targeted dyes signifies the first order kinetics with corresponding R^2 value of 0.9948 and 0.9937 respectively. Also, the corresponding degradation rate constants for the decomposition of CV and VB were 0.0454 min^{-1} and 0.0474 min^{-1} respectively.

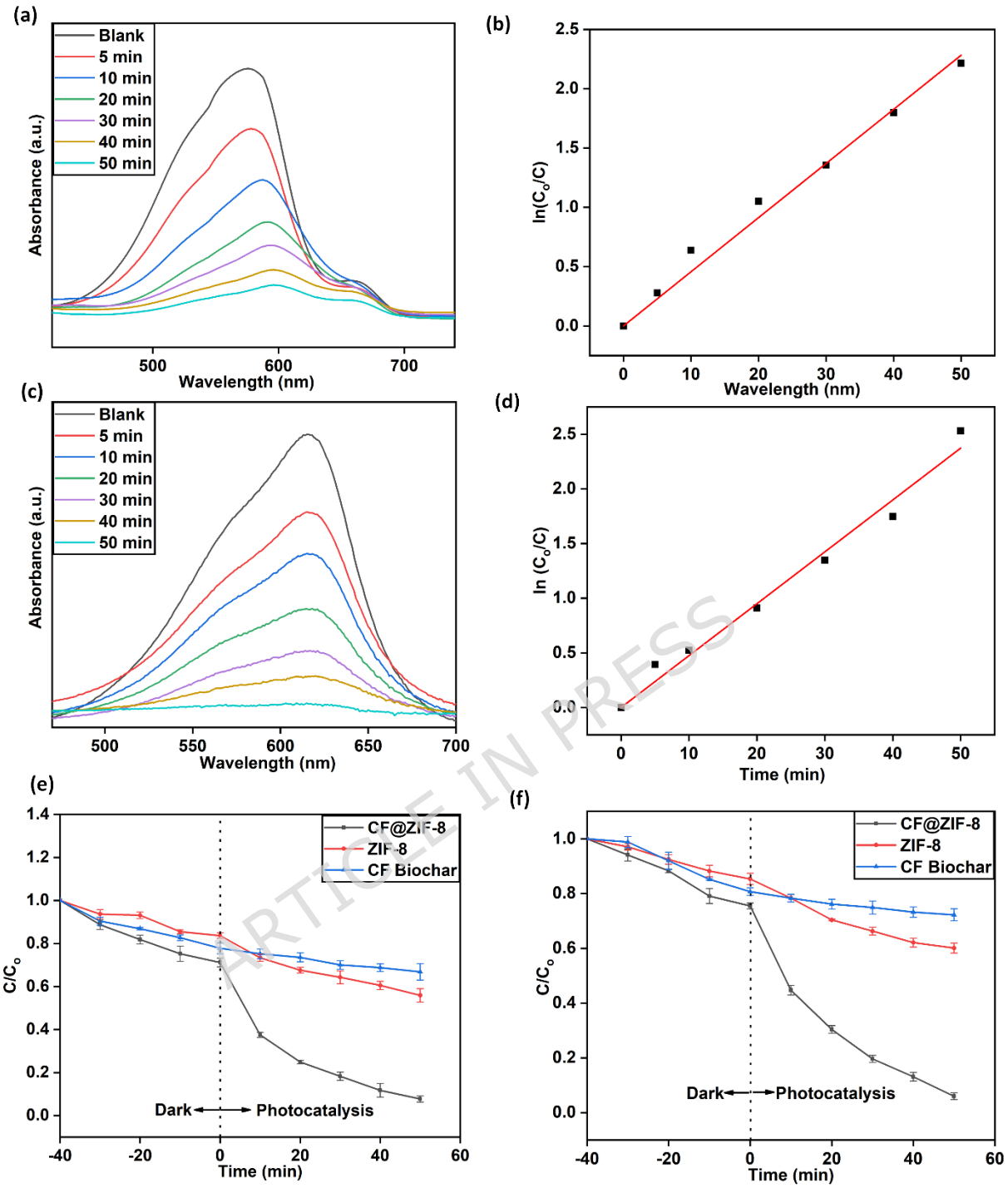

Fig 10: (a) Photocatalytic breakdown profile of CV by CF-ZIF-8 catalyst under optimised conditions; (b) Corresponding degradation kinetics, $\ln(C_o/C)$ vs time plot for photocatalytic degradation of CV under optimised conditions; (c) Photocatalytic breakdown profile of VB by CF-ZIF-8 catalyst under optimised conditions; (d) Corresponding degradation kinetics,

ln(C_o/C) vs time plot for photocatalytic degradation of VB under optimised conditions; (e) Photocatalytic breakdown analysis of CV in presence of different catalytic environment and (f) Photocatalytic breakdown analysis of VB in presence of different catalytic environment.

Table 1: Various catalyst used in the photocatalytic degradation of CV and VB

Catalyst	**Contaminant**	**Irradiation Time (min)**	**Source of illumination**	**Removal Percentage (%)**	**References**
SnO_2/ZnO	CV	75	UV light	90	[74]
ZnO-nanoflowers	CV	120	UV light	90	[75]
BISe-CM	CV	150	Solar Irradiatiom	Complete Degradation	[71]
RGO-$ZnFe_2O_3$	CV	60	Visible light	90	[76]
CF-ZIF-8	CV	50	Sunlight	89 ± 1.21%	**This work**
Fe_3O_4@LP-Ag	VB	100	Sunlight	94	[77]
CuO NPs	VB	42	UV-Visible irradiation	>90	[78]

V_2O_5 nanorods/GO	VB	90	Sunlight irradiation	97.95	[79]
CF-ZIF-8	VB	50	Sunlight irradiation	92 ± 1.57%	**This work**

4.6. Investigation of the photocatalytic performance of CF-ZIF-8 catalyst for the presence of different inorganic ions present in water

There is insufficient understanding regarding the role played by different inorganic ions in the photocatalytic decomposition of organic pollutants. In view of possible real world significance, this study explored the impact exerted by different inorganic ions during the photocatalytic decolorization of the two dyes viz CV and VB. The occurrence of multiple inorganic ions with their complex impact impedes the real world application of photocatalyst during photocatalytic degradation[80]. For the synthesized material to reach the commercial viability, it must function robust behaviour under challenging environments, given that the habitant of different inorganic species exert potential inhibitory influence of the photocatalytic degradation efficiency. In order to study the influence exerted by these ions, 0.01 M concentration of different inorganic salts of the ions Al^{3+}, Na^{+}, Mg^{2+}, F^{-}, SO_4^{2-} and Cl^{-} were separately added under optimal conditions into distinct batches of the reaction mixture.

4.6.1. Influence of Cations

As the cations such as Al^{3+}, Na^{+} and Mg^{2+} being in their most stable oxidation states, they are generally considered to exert negligible impact on the photocatalysis process[81]. On the basis of the results furnished by **Fig 11(a)** and **Fig11(b)**, the photocatalytic decolourization of the targeted pollutants were distinctly affected by the impact of different cations to varying magnitude. For the dye solutions containing Al^{3+} ion, a substancial decline in the removal efficiency of the dyes were observed, likely due to the intense charge density of the Al^{3+} ions and strong tendency to adhere on the photocatalyst's surface[82]. The Al^{3+} ions also hinder the formation of reactive oxygen species (ROS) by blocking the photocatalyst's active sites and therefore suppressing their accessibility. The modest drop observed in the degradation percentage of both the dye solutions comprising of Mg^{2+} and Na^{+} ions may account for the suppressive effect caused by the presence of Cl^{-} ions in the solutions. Cl^{-} ions are known to disrupt the photocatalytic decolorization efficiency by competing with the molecules of the contaminants and limiting their access to the active sites and by diminishing the formation of active species and holes present in the valence band that are responsible for the photodegradation process[83].

4.6.2. Influence of Anions

Wastewater is also known to constitute diverse inorganic anions that are known to suppress the generation of photogenerated ROS and impede the overall degradation of organic contaminants. The results furnished in **Fig 11(c)** and **Fig 11(d)** reveal the extent of impact exerted by different anions on the photocatalytic decolourization of the pollutants under investigation. The inhibitory effect exerted by the presence of different anions in the

decolourization of CV and VB follows the trend $Cl^- > SO_4^{2-} > F^-$. Two foremost reasons can satisfactorily account for the observed drop of the degradation efficiency. These anions cause blockage in the availability of the active sites of the catalyst and in turn reduces the formation of light induced active species and also due to the quenching behaviour exerted by these anions. The presence of Cl^- ions exerted a negative impact on the photocatalytic performance thus reducing the effective elimination of CV and VB. Due to their negative charge they interacted readily with the h^+ and $^{\cdot}OH$ radicals and caused their effective quenching. The outcome of these reactions was the formation of weakly reactive $Cl^{\cdot}$ radicals that slowed the decolourization of CV and VB[84]. When compared with $^{\cdot}OH$ radicals the reactive ability of $Cl^{\cdot}$ radicals is weak and slows the process of elimination of targeted molecules[85]. Furthermore, by adsorbing on the photocatalyst surface, the Cl^- ions obstruct the active regions of the photocatalyst and interferes with the interaction of pollutant molecules with the active regions. Consequently the Cl^- ions functions the quenching of the the reactive species that take part in the degradation process [86].

$$Cl^- + h^+ \longrightarrow Cl^{\cdot} \quad (6)$$

$$Cl^- + {}^{\cdot}OH \longrightarrow HClO^{-\cdot} \quad (7)$$

$$HClO^{-\cdot} + H^+ \longrightarrow Cl^{\cdot} + H_2O \quad (8)$$

$$Cl^{\cdot} + Cl^- \longrightarrow Cl_2^{-\cdot} \quad (9)$$

It is reflected from the **Fig 11(c)** and **Fig 11(d)**, the sulfate radicals also has an inhibitory effect during the photocatalytic decomposition of CV and VB. This behaviour of sulfate ions can be likely because of the high affinity

of the sulfate ions for adsorption on the photocatalyst surface and also due to their tendency to undergo quenching interactions with h^+ and $^{\cdot}OH$ radicals[87]. The various interaction of SO_4^{2-} radicals responsible for reducing the photocatalytic decolourization of CV and VB are explained by the following equations[88]:

$$SO_4^{2-} + h^+ \longrightarrow SO_4^{\cdot -} \quad (10)$$

$$SO_4^{2-} + {}^{\cdot}OH \longrightarrow SO_4^{\cdot -} + OH^- \quad (11)$$

$$SO_4^{\cdot -} + e^- \longrightarrow SO_4^{2-} \quad (12)$$

The F^- exerted minimum influence in the photocatalytic elimination of the targeted contaminants. Because of their stability, small size and resistive oxidisable nature they tend to accumulate on the photocatalyst surface and supres the generation of $^{\cdot}OH$ radicals[89].

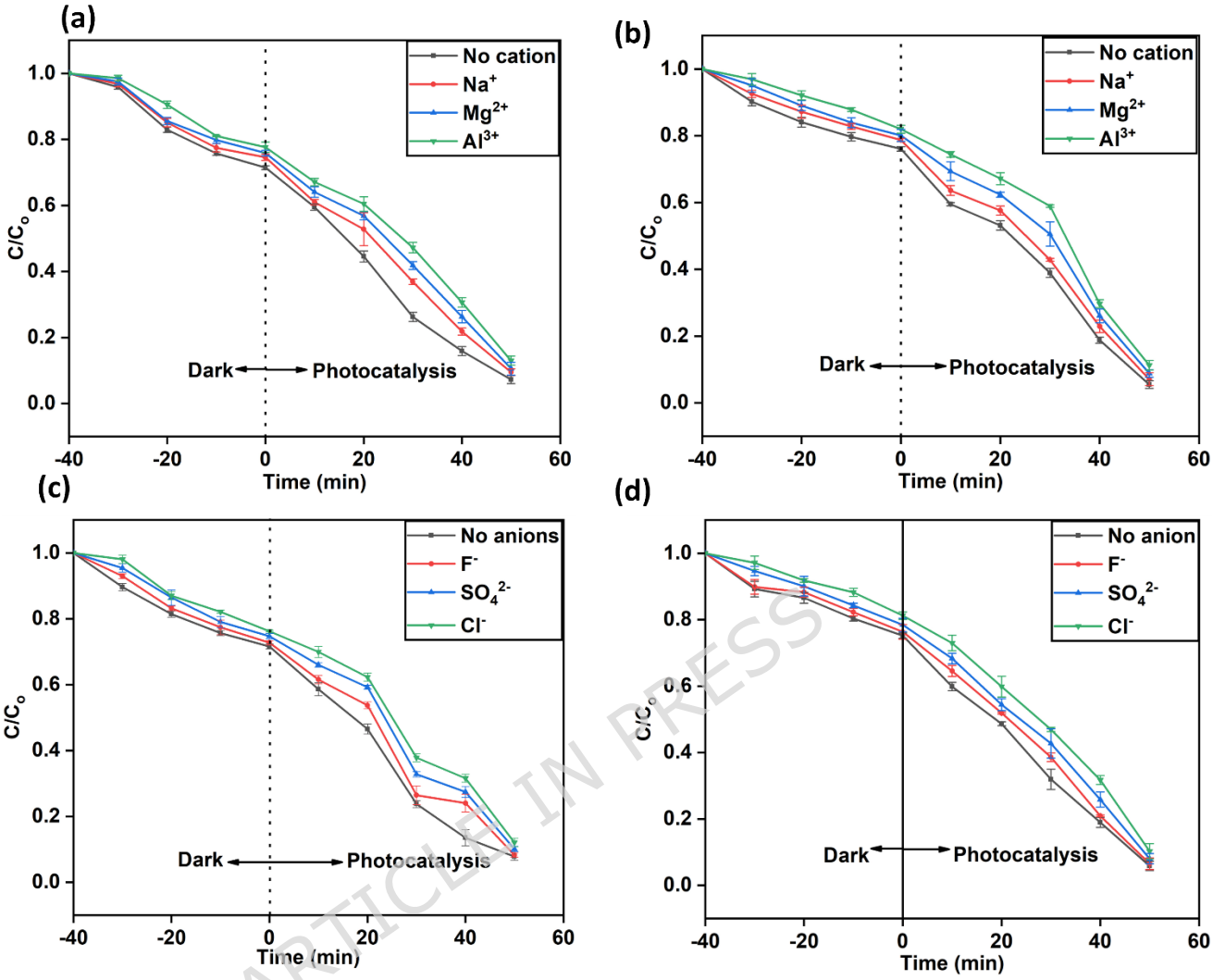

Fig 11: (a)Influence of different cations on the photocatalytic degradation of CV; (b) Influence of different cations on the photocatalytic degradation of VB; (c) Influence of different anions on the photocatalytic degradation of VB; (d) Influence of different anions on the photocatalytic degradation of VB

4.7. Impact of various water matrices

For supporting the robustness of the photocatalytic degradation process for the treatment of real world waste water sample, the degradation of CF-ZIF-8 was conducted with four distinct sources of water samples. To understand the influence of different types of water on the removal rate of the studied

pollutants, four various water samples originated from different water sources were studied including the mineral water, lake water, tap water and distilled water. The trends in the removal percentage of the investigated pollutants for four different water samples are displayed in **Fig 12(a)**. Except in distilled water sample, there was a marginal suppression of the photocatalytic removal percentage in case of the other water samples. Such a minimal suppression of the degradation efficiency can be linked due to the existence of multiple inorganic and organic constituents in the water samples[90]. The degradation percentage was also less affected in case of mineral water as it contains very minimal percentage of impurities and dissolved oxygen matter. Tap water and lake water on the other hand includes a wide variation of additional organic constituents and co-existing ions that led to suppressive behavior of the degradation of the studied pollutants. The overall suppresion in the degradation behaviour of the CF-ZIF-8 catalyst in different aqueous environment can mainly occur due to two basic reasons: refraction in the penetration of the light and inhibition of the photocatalytic efficiency because of the presence of several organic moieties and inorganic ions to different extent in the studied samples of water[63].

4.8. Mechanistic Insights for the photocatalytic removal of the targeted pollutants

4.8.1. Scavenger Test

It is well understood that the photodegradation efficiency is strongly influenced by the quantity of ROS (reactive oxygen species) formed within the degradation process and also on the generation of the electron-hole pair

during photocatalysis. The influence of the e^- , h^+ and ROS on CV and VB degradation were evaluated by the introduction of different scavenging agents that can capture these radicals and charge carriers and identify which amongst them plays a predominant role in the breakdown of the targeted pollutants. Several sacrificial compounds such as EDTA, ascorbic acid, $K_2S_2O_8$ and 2-butanol were used for trapping h^+, $\cdot O_2^-$, e^- and $\cdot OH$ radicals[72]. As per **Fig 12(b)**, after adding 1 mM of the respective trapping agents, the degradation efficiency of CV and VB decreased as 61 ± 2.20% and 68 ± 2.12% in presence of EDTA, 40 ± 1.4% and 47 ± 1.4% for the 2-butanol solution, 71 ± 1.41% and 76 ± 2.12% in case of $K_2S_2O_8$ and 49 ± 0.70% and 53 ± 1.41% in presence of ascorbic acid. The degradation rate of CV and VB was only marginally decreased in case of $K_2S_2O_8$ and EDTA, **Fig 12(b)**. Therefore from the above results it is clear that the $\cdot OH$ and $\cdot O_2^-$ played a predominant role during the photocatalytic breakdown of the targeted pollutants.

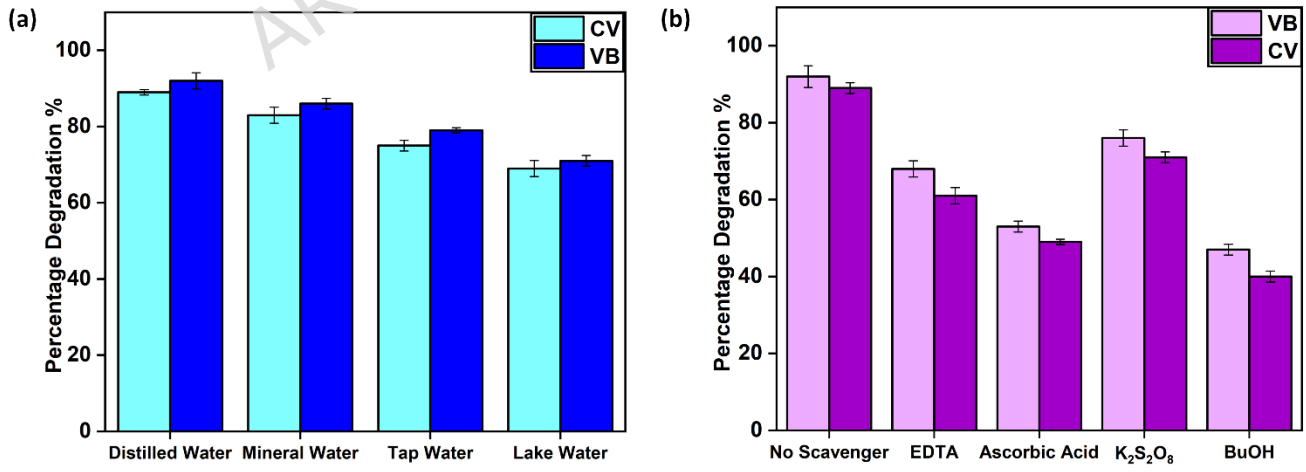

Fig 12: (a) Study of photocatalytic breakdown of the investigated dyes in presence of various water matrices; (b) Influence of different radical

scavengers on the photocatalytic degradation profile of the investigated dyes.

4.8.2. Formation of strongly oxidising ·OH radicals

Monitoring the production of ·OH radicals is vital as they are the key contributors for the photocatalytic breakdown of the pollutant molecules. The photoluminescence measurements evidenced the production of these radicals. The detection of ·OH radicals wes verified using terephthalic acid (TA) as a fluorescent probe that gives 2-hydroxyterephthalic acid after interacting with ·OH radicals. Due to the fluorescence properties of 2-hydroxyterephthalic acid, it emits a high intensity signal at ~420 nm[91]

$$TA \xrightarrow{\cdot OH} TAOH \quad (13)$$

For this, an aqueous solution of 0.5 mM TA was added under optimized reaction parameters to 35 ml of the targeted dye solutions. The solution was initially placed in dark conditions to reach adsorption equilibrium before illuminated under solar light. PL spectra was recorded by extracting 1.5 ml of aliquot solution periodically and exciting at 315 nm wavelength, **Fig 13(a)** and **Fig 13(b)**. The rising peak intensity illustrates the formation of ·OH radicals during the degradation.

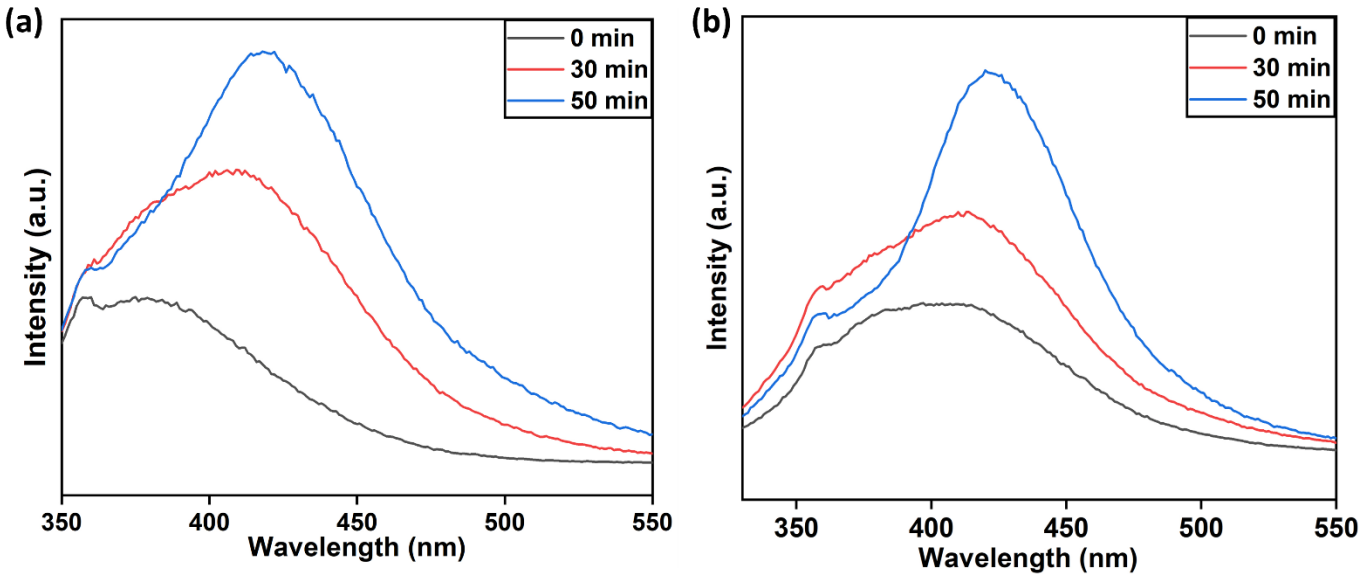

Fig 13: (a) PL spectrum showing the formation of ˙OH radicals during the photocatalytic breakdown of CV and (b) PL spectrum showing the formation of ˙OH radicals during the photocatalytic breakdown of VB

4.9. Plausible Mechanistic Pathway for removal of the targeted dye molecules

On the basis of the above experimental results, the photodegradation of CV and VB may occur through two possible pathways as stated in the **Fig 14**. According to the first proposed mechansim, at the first stage the CF-biochar captures the targeted dye molecules owing to its well developed porous structure and occurrence of plentiful functional groups on the surface. This provides more contact between the contaminant molecules and the catalyst surface. Such abundant occurence of different functional groups facilitates the pollutant-catalyst interaction through different forces such as electrostatic force[92], pore filling[93] and hydrogen bonding[94]. Also the presence of several aromatic rings in the biochar matrix enhances the pollutant-catalyst interaction and boost the photocatalytic breakdown of the

pollutant molecules[95]. The irradiation of solar light, causes the photoexcitation of the CF-ZIF-8 catalyst thus promoting the electrons belonging to the valence band (VB) to transfer to the conduction band (CB). This also lead to the generation of h^+ in the valence band. Subsequently, the biochar matrix assists the electron transfer and functions as the electron carrier, preventing the e^--h^+ pair recombination[96]. Such extended lifespan of the charge carriers, results in greater photocatalytic performance of the CF-ZIF-8 catalyst as it promotes the generation of highly active free radicals (·OH and $·O_2^-$) that drive the breakdown of the dye molecules. The interaction between e^- of the conduction band with O_2 molecules dissolved in the solution causes the formation of highly active $·O_2^-$ radicals. Also the interaction between the h^+ of the valence band and H_2O molecule produces ·OH radicals[97]. The $·O_2^-$ and ·OH radicals so formed are highly reactive in nature and ultimately lead to the breakdown of the pollutant molecules. The key reactions that led to the degradation of the pollutant molecules are as follows:

$$\text{CF@ZIF-8} \xrightarrow{+\ h\nu} e^- + h^+ \quad (14)$$

$$h^+ \xrightarrow{+\ H_2O} OH^- + H^+ \quad (15)$$

$$h^+ + OH^- \longrightarrow ·OH \quad (16)$$

$$e^- + O_2 \longrightarrow ·O_2^- \quad (17)$$

$$·O_2^- \xrightarrow{+\ H^+} HO_2· \quad (18)$$

$HO_2^{\cdot} + e^- \longrightarrow HO_2^{\cdot -}$ (19)

$HO_2^{\cdot -} + H^+ \longrightarrow H_2O_2$ (20)

$H_2O_2 + e^- \longrightarrow {}^{\cdot}OH + OH^-$ (21)

CV/VB + ${}^{\cdot}OH \longrightarrow$ Degraded Products (22)

Furthermore, the simultaenous dye-sensitization can also significantly contribute to the photocatalytic degradation of CV and VB. The dye molecules during the illumination of sunlight can absorb the visible radiations to cause photoexcitation of e^- from HOMO (highest occupied molecular orbital) to LUMO (lowest unoccupied molecular orbital). These excited e^- can jump from the LUMO of the excited dye molecules to the photocatalyst's conduction band. The superior e^- transport of the biochar matrix facilitates the migration of these e^- from the conduction band towards the photocatalyst surface. These e^- present on the photocatalyst surface can produce ${}^{\cdot}O_2^-$ radicals upon interaction with O_2 molecules which ultimately causes the mineralization of the dye molecules[98-99]. The reactions involved in the dye sensitized degradation of CV/VB are stated below.

Dye + $h\nu \longrightarrow$ Dye* (Photosensitized) $(h^+_{HOMO} + e^-_{LUMO})$ (23)

Dye* + CF@ZIF-8 $\longrightarrow$ Dye* (h^+_{HOMO}) + CF@ZIF-8 (e^-_{CB}) (24)

CF@ZIF-8 (e^-_{CB}) $\xrightarrow{+\ O_2}$ $\cdot O_2^-$

(25)

$\cdot O_2 + 2H^+ \xrightarrow{+\ 2e^-} H_2O_2$

(26)

$H_2O_2 + \cdot O_2^- \longrightarrow \cdot OH + OH^- + O_2$

(27)

$\cdot OH + CV/VB \xrightarrow{(Dye)}$ Degraded Products

(28)

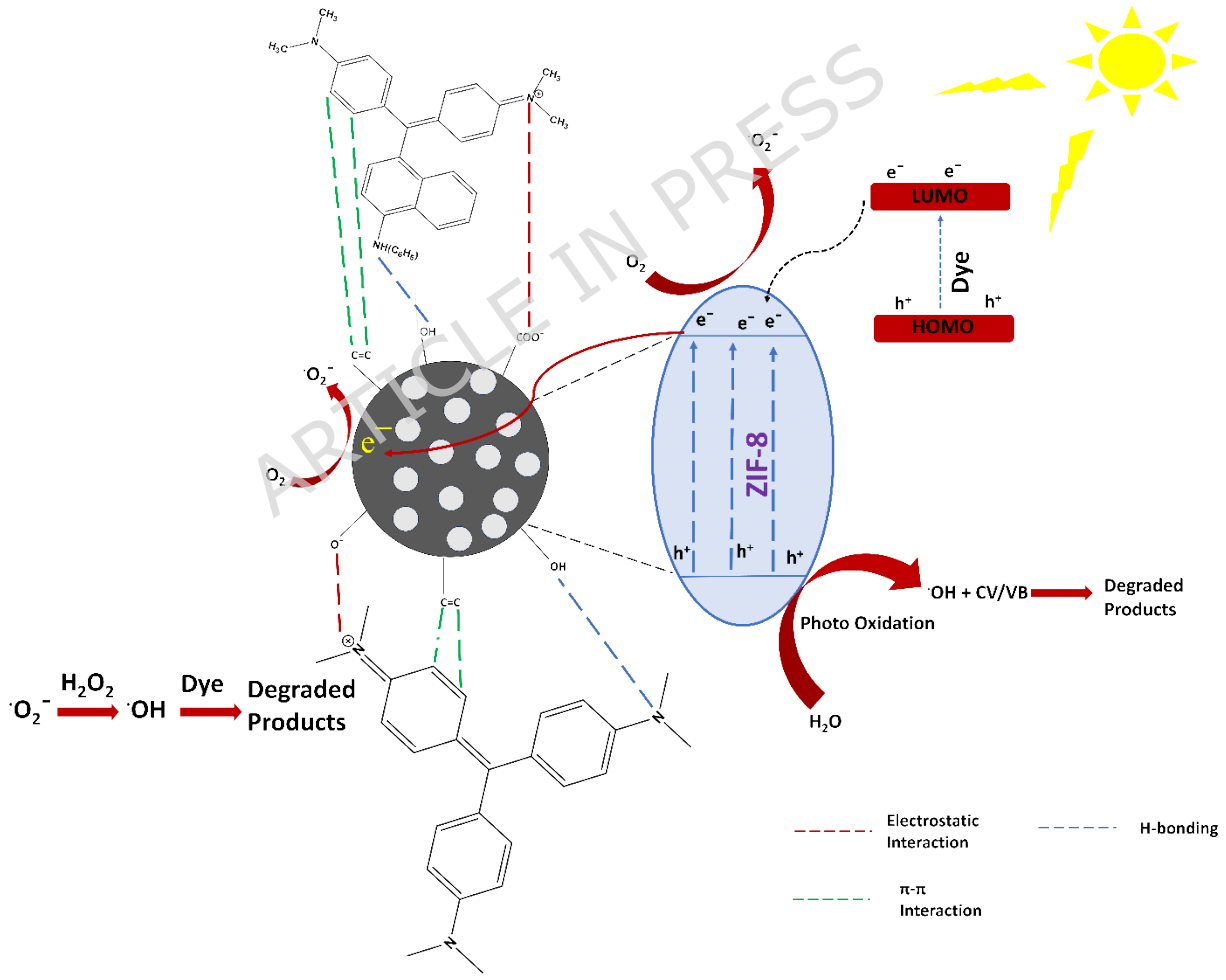

Fig 14: Possible mechanistic pathway for the photocatalytic breakdown of the investigated dyes

Additionally, further evidence of the photocatalytic mechanistic pathway for the photocatalytic degradation of CV and VB was also evaluted through LC-MS (Liquid Chromatography-Mass Spectroscopy) analysis. LC-MS was conducted inorder to investigate the intermediate products formed during degradation of CV and VB. Fig 15 presents the tentative degradation mechanistic insights for the degradation of VB. Fig S1 presents the LCMS spectrum for the degradation of VB. In presence of the sunlight irradiation the ·OH radical generated in the reaction serves as the primary reactive species that triggers the breakdown of VB through oxidative degradation, N-dealkylation, aromatic ring opening and breakdown of C-C and C-N bond. The oxidative degradation by the ·OH radical results in the formation of the intermediate at m/z at 299. The demethylation, aromatic ring opening and breaking of C-C bond gives the intermediate at m/z = 225 which finally undergoes oxidative degradation resulting in the fragments at m/z = 121 and 106. The intermediate peak at m/z = 352 is formed by the breaking of C-C bond that finally undergoes oxidative degradation resulting in the intermediates at m/z = 318 and 235. These intermdiates than finally undergoes ring opening of the aromatic structure to result the intermediates at m/z = 173, 282 and 135 that finally undergoes mineralizarion producing CO_2 and H_2O[100]. Similarly Fig 16, presents the speculated mechanistic pathway for the degradation of CV on the basis of the LCMS spectrum in Fig S2. There are two possible mechanistic pathway for breakdown of CV. The oxidative degradation by the ·OH radicals results in the formation of the intermediate framgment at m/z = 268, subsequent

demethylation and ring opening results in the formation of the other intermediate fragments at m/z values 240, 226, 177, 135, 100 and 118 which finally results in the mineralization of dye producing CO_2 and water. The second route involves the demethylation in the aromatic framework, followed by the oxidative degradation by the $^{\cdot}OH$ radical and ring opening finally leading to minerization. This route involves the formation of the intermediate peak at m/z values 358, 330, 316, 302, 288.

4.10. Recyclability

The photocatalyst stability is a crucial parameter for the photocatalytic breakdown of harmful organic pollutant molecules[101]. In this study, CF-ZIF-8 was chosen for the photocatalytic breakdown of the dyes under analysis under sunlight irradiation for five consecutive photocatalytic runs and the results obtained are furnished in **Fig 15(a)**. After each run, the CF-ZIF-8 catalyst was recovered from the solutions by centrifugation and reused for the succeeding run after drying at 70° C[102]. The CF-ZIF-8 catalyst showed an initial removal percentage of 92 ± 1.57% and 89 ± 1.21% for VB and CV in the first catalytic cycle. However there was a marginal decrease in the photocatalytic removal percentage of CF-ZIF-8 catalyst till the fourth catalytic run.

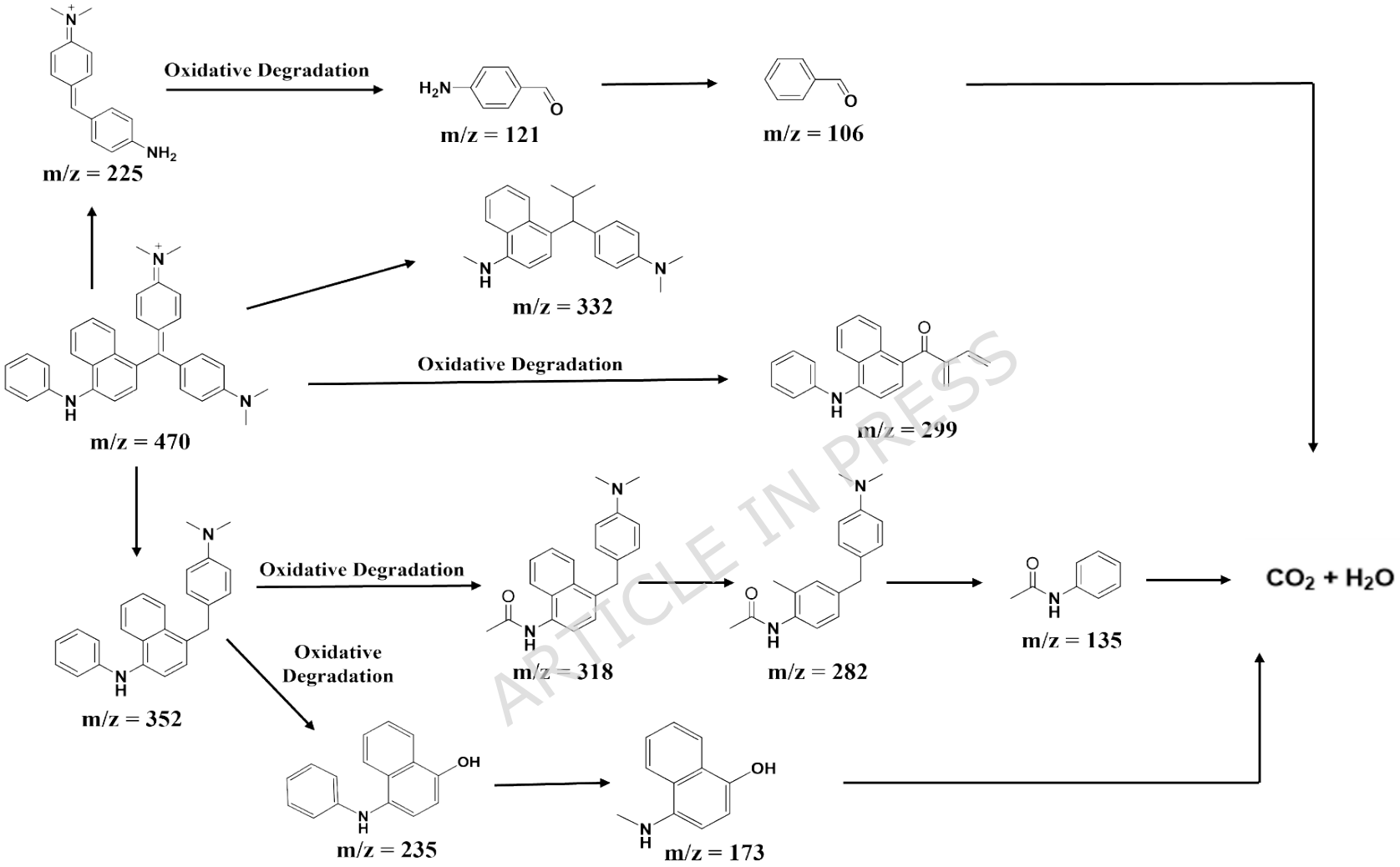

Fig 15: Tentative mechanistic pathway for the degradation of VB

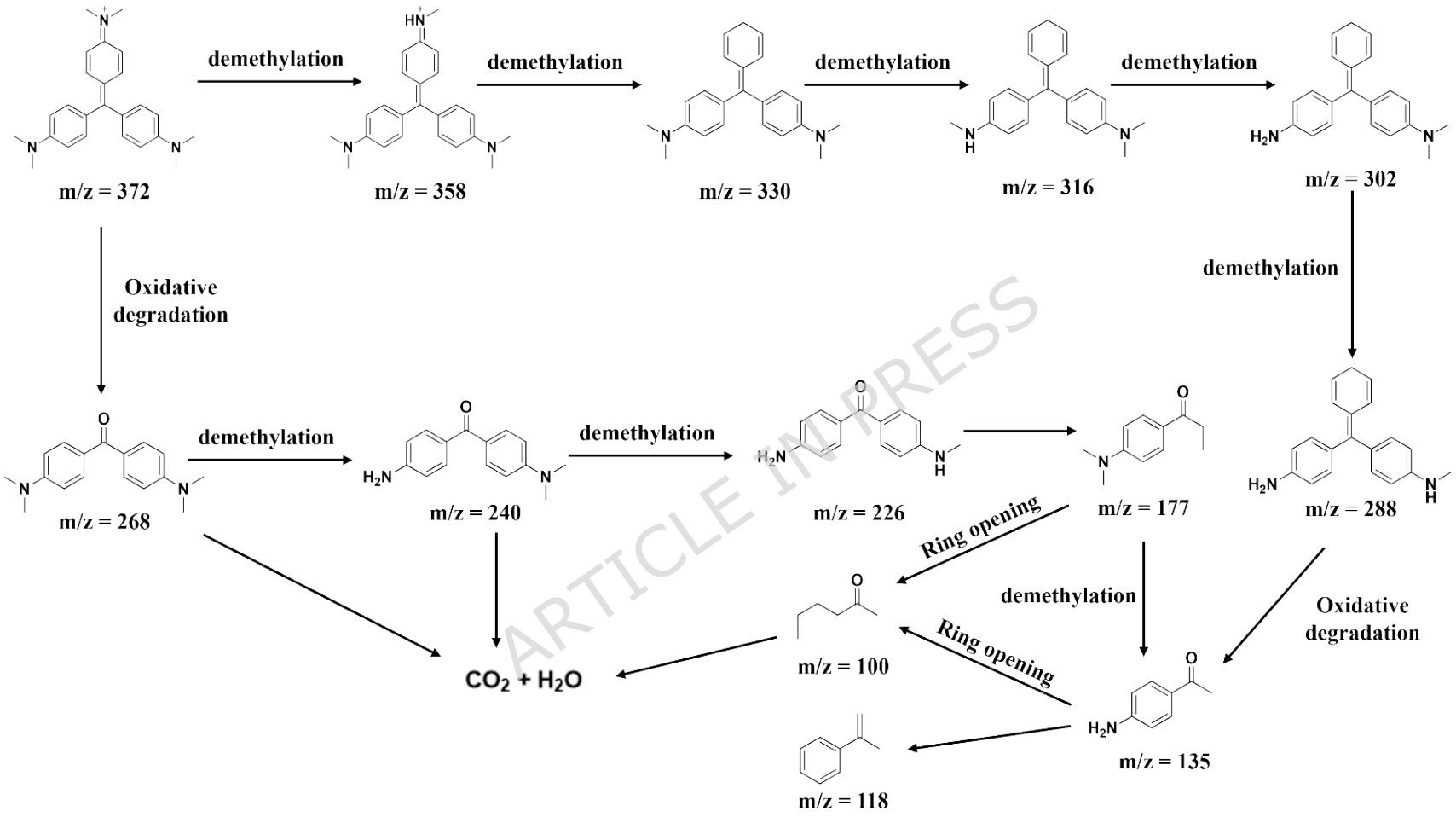

Fig 16: Tentative mechanistic pathway for the degradation of CV

The degradation percentage of VB and CV after the fourth run was 87 ± 0.7% and 83 ± 2.12%, relative to the initial photodegradation cycle, there was only 5% and 6% drop in the removal percentage by CF-ZIF-8 catalyst. Additionally, in order to evaluate the structural integrity of the CF-ZIF-8 catalyst, PXRD analysis was performed for the regenerated CF-ZIF-8 catalyst. There was no characteristic change in the PXRD pattern, **Fig 15(b)** of the reused CF-ZIF-8 catalyst was seen which reflected that the CF-ZIF-8 catalyst maintained its structural integrity even after successive use.

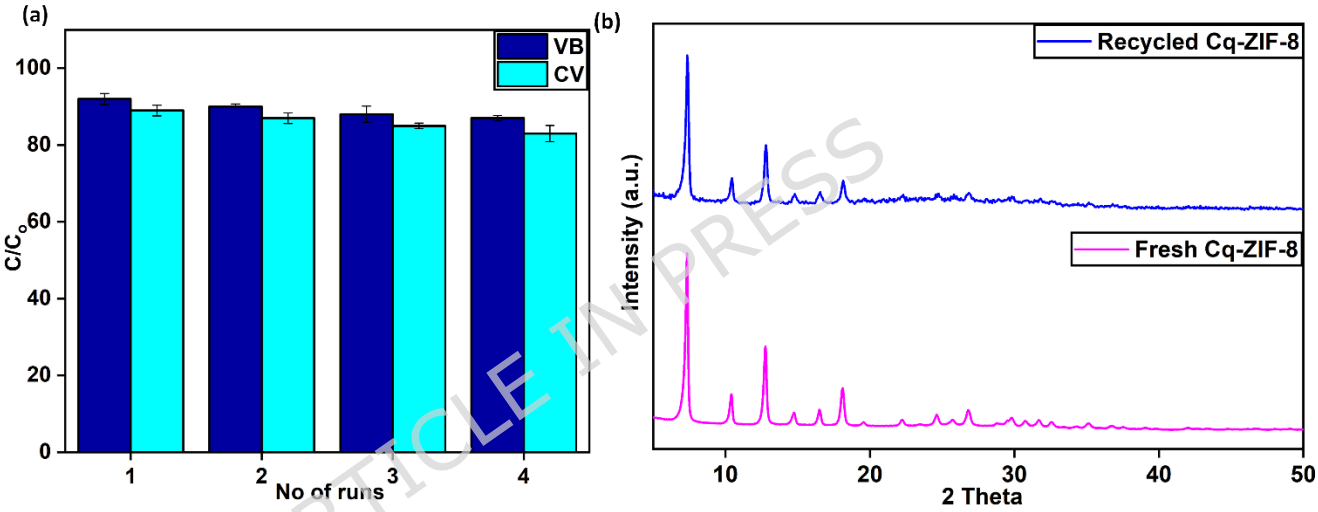

Fig 15: (a) Reusability investigations of CF-ZIF8 catlyst; (b) Comparison of the PXRD pattern of the reused CF-ZIF-8 catalyst with the PXRD pattern of the fresh CF-ZIF-8.

5. Conclusion

This work describes a sustainable way for the effective utilization of biomass wastes by processing cauliflower wastes into biochar. The biochar obtained by the pyrolysis of biomass of cauliflower leaves was further used for the modification of ZIF-8 for the fabrication of a cost efficient composite. The

successful linking of the CF biochar to ZIF-8 surface was confirmed by different analytical techniques including IR, PXRD, TEM, XPS, UV-DRS and PL analysis. The CF-ZIF-8 catalyst demonstrated strong photocatalytic decomposition of CV (89 ± 1.21%) and VB (92 ± 1.57%) in presence of sunlight irradiation for 50 minutes of time period. These results, surpasses the degradation performance exerted by ZIF-8 alone which reflects the presence of synergistic influence between the ZIF-8 and CF biochar influencing the degradation efficiency. Such boost in the photocatalytic performance is mainly attributed to the highly porous nature of the material and mobility of the photoinduced charge carriers. Additionally from the scavenger test analysis, photoinduced $^{\cdot}OH$ and $^{\cdot}O_2^-$ radicals are the key contributors for oxidizing the pollutant molecules as explained in the photodegradation mechanism. The CF-ZIF-8 catalyst also maintained its degradation efficiency with a minimal drop till the fourth catalytic cycle. However, such a drop in degradation efficiency of the photocatalyst also limits the application of the photocatalyst for more subsequent cycles thereby reducing the economic utility of the material. In this paper we have limited our study only with a single quantity of biochar (400mg) compositing with ZIF-8, this widens the scope to study the influence on the photocatalytic degradation of the contaminants by varying the quantity of biochar forming composite with ZIF-8. Moreover, in the recent years the application of biochar as a valuable resource has drawn tremendous recognition due to their natural availability. This study broadens the boundaries for the development of cost effective photocatalyst of ZIF-8 with biochar originating from diverse sources for wastewater remediation.

Availability of data and materials

All data generated or analyzed during this study are included in this published article.

Declaration of Competing Interest

The authors declare that they have no known competing financial interests or personal relationships that could have appeared to influence the work reported in this paper.

Funding

Not applicable

Authors' contributions

“J. D. and M. A. wrote the main manuscript text, commented, revised and corrected the whole manuscript. B.H. commented and corrected the manuscript. All authors reviewed the manuscript."

Acknowledgments

The authors are thankful to the Director, National Institute of Technology, Silchar, for his help and continuous support in preparing the manuscript.

6. References

1. Lu, F. & Astruc, D. Nanocatalysts and other nanomaterials for water remediation from organic pollutants. *Coord. Chem. Rev.* **408**, 213180 (2020).
2. Benkhaya, S., M’rabet, S. & El Harfi, A. A review on classifications, recent synthesis and applications of textile dyes. *Inorg. Chem.*

Commun. **115**, 107891 (2020).

3. Rafatullah, M., Sulaiman, O., Hashim, R. & Ahmad, A. Adsorption of methylene blue on low-cost adsorbents: a review. *J. Hazard. Mater.* **177**, 70–80 (2010).
4. Ogugbue, C. J. & Sawidis, T. Bioremediation and detoxification of synthetic wastewater containing triarylmethane dyes by Aeromonas hydrophila isolated from industrial effluent. *Biotechnol. Res. Int.* **2011**, 967925 (2011).
5. Nasar, A. & Mashkoor, F. Application of polyaniline-based adsorbents for dye removal from water and wastewater—a review. *Environ. Sci. Pollut. Res.* **26**, 5333–5356 (2019).
6. Von Lau, E., Gan, S., Ng, H. K. & Poh, P. E. Extraction agents for the removal of polycyclic aromatic hydrocarbons (PAHs) from soil in soil washing technologies. *Environ. Pollut.* **184**, 640–649 (2014).
7. Deering, K., Spiegel, E., Quaisser, C., Nowak, D., Rakete, S., Garí, M., & Bose-O'Reilly, S. Exposure assessment of toxic metals and organochlorine pesticides among employees of a natural history museum. *Environ. Res.* **184**, 109271 (2020).
8. Lellis, B., Fávaro-Polonio, C. Z., Pamphile, J. A. & Polonio, J. C. Effects of textile dyes on health and the environment and bioremediation potential of living organisms. *Biotechnol. Res. Innov.* **3**, 275–290 (2019).
9. Betancur, S. B., Gil, S. A., Ardila, A. A. N., Arriola, V. E., Barrera, Z. R., Hernández, J. A., & Zepeda, T. A. Developing bioadsorbents from orange peel waste for treatment of raw textile industry wastewater.

Desalin. Water Treat. **250**, 80–99 (2022).

10. Zahrani, A. A. & Ayati, B. Using heterogeneous Fe-ZSM-5 nanocatalyst to improve the electro Fenton process for acid blue 25 removal in a novel reactor with orbiting electrodes. *J. Electroanal. Chem.* **873**, 114456 (2020).
11. Ejhieh, A. N. & Khorsandi, M. Photodecolorization of Eriochrome Black T using NiS–P zeolite as a heterogeneous catalyst. *J. Hazard. Mater.* **176**, 629–637 (2010).
12. Ikram, M., Raza, A., Imran, M., Ul-Hamid, A., Shahbaz, A., & Ali, S. Hydrothermal synthesis of silver decorated reduced graphene oxide (rGO) nanoflakes with effective photocatalytic activity for wastewater treatment. *Nanoscale Res. Lett.* **15**, 1–11 (2020).
13. Aramendía, M. A., Marinas, A., Marinas, J. M., Moreno, J. M. & Urbano, F. J. Photocatalytic degradation of herbicide fluroxypyr in aqueous suspension of TiO2. *Catal. Today* **101**, 187–193 (2005).
14. Lee, Y.Y., Moon, J.H., Choi, Y.S., Park, G.O., Jin, M., Jin, L.Y., Li, D., Lee, J.Y., Son, S.U. & Kim, J.M. Visible-light driven photocatalytic degradation of organic dyes over ordered mesoporous Cd x Zn1–x S materials. *J. Phys. Chem. C* **121**, 5137–5144 (2017).
15. Shahwan, T., Sirriah, S. A., Nairat, M., Boyacı, E., Eroğlu, A. E., Scott, T. B., & Hallam, K. R. Green synthesis of iron nanoparticles and their application as a Fenton-like catalyst for the degradation of aqueous cationic and anionic dyes. *Chem. Eng. J.* **172**, 258–266 (2011).
16. Shams-Ghahfarokhi, Z. & Nezamzadeh-Ejhieh, A. As-synthesized ZSM-5 zeolite as a suitable support for increasing the photoactivity of

semiconductors in a typical photodegradation process. *Mater. Sci. Semicond. Process.* **39**, 265–275 (2015).

17. Fujishima, A. & Honda, K. Electrochemical photolysis of water at a semiconductor electrode. *Nature* **238**, 37–38 (1972).
18. Dong, C., Ji, J., Yang, Z., Xiao, Y., Xing, M., & Zhang, J. Research progress of photocatalysis based on highly dispersed titanium in mesoporous SiO_2. *Chinese Chem. Lett.* **30**, 853–862 (2019).
19. Liang, H., Hua, P., Zhou, Y., Fu, Z., Tang, J., & Niu, J. Fabrication of Cu/rGO/MoS_2 nanohybrid with energetic visible-light response for degradation of rhodamine B. *Chinese Chem. Lett.* **30**, 2245–2248 (2019).
20. Li, G., Nie, X., Gao, Y. & An, T. Can environmental pharmaceuticals be photocatalytically degraded and completely mineralized in water using g-C_3N_4/TiO_2 under visible light irradiation?—Implications of persistent toxic intermediates. *Appl. Catal. B Environ.* **180**, 726–732 (2016).
21. Xue, Y., Chang, Q., Hu, X., Cai, J. & Yang, H. A simple strategy for selective photocatalysis degradation of organic dyes through selective adsorption enrichment by using a complex film of CdS and carboxylmethyl starch. *J. Environ. Manage.* **274**, 111184 (2020).
22. Miao, J., Lu, H., Habibi, D., Khiadani, M. H. & Zhang, L. Photocatalytic degradation of the azo dye acid red 14 in nanosized TiO_2 suspension under simulated solar light. *CLEAN–Soil, Air, Water* **43**, 1037–1043 (2015).
23. Qiu, J., Zhang, X., Feng, Y., Zhang, X., Wang, H., & Yao, J. Modified metal-organic frameworks as photocatalysts. *Appl. Catal. B Environ.*

231, 317–342 (2018).

24. Yaghi, O. M., Li, G. & Li, H. Selective binding and removal of guests in a microporous metal–organic framework. *Nature* **378**, 703–706 (1995).
25. Furukawa, H., Cordova, K. E., O'Keeffe, M. & Yaghi, O. M. The chemistry and applications of metal-organic frameworks. *Science* **341**, 1230444 (2013).
26. Wei, Z., Ding, B., Dou, H., Gascon, J., Kong, X.J., Xiong, Y., Cai, B., Zhang, R., Zhou, Y., Long, M. & Miao, J. 2020 roadmap on pore materials for energy and environmental applications. *Chinese Chem. Lett.* **30**, 2110–2122 (2019).
27. Filippousi, M., Turner, S., Leus, K., Siafaka, P.I., Tseligka, E.D., Vandichel, M., Nanaki, S.G., Vizirianakis, I.S., Bikiaris, D.N., Van Der Voort, P. & Van Tendeloo, G. Biocompatible Zr-based nanoscale MOFs coated with modified poly (ε-caprolactone) as anticancer drug carriers. *Int. J. Pharm.* **509**, 208–218 (2016).
28. Alvaro, M., Carbonell, E., Ferrer, B., Llabrés i Xamena, F. X. & Garcia, H. Semiconductor behavior of a metal-organic framework (MOF). *Chem. Eur. J.* **13**, 5106–5112 (2007).
29. Llabrés i Xamena, F. X., Corma, A. & Garcia, H. Applications for metal− organic frameworks (MOFs) as quantum dot semiconductors. *J. Phys. Chem. C* **111**, 80–85 (2007).
30. Nasalevich, M. A., Van der Veen, M., Kapteijn, F. & Gascon, J. Metal–organic frameworks as heterogeneous photocatalysts: advantages and challenges. *CrystEngComm* **16**, 4919–4926 (2014).

31. Xia, T., Lin, Y., Li, W. & Ju, M. Photocatalytic degradation of organic pollutants by MOFs based materials: A review. *Chinese Chem. Lett.* **32**, 2975–2984 (2021).

32. Liu, M., Gao, Y., Wang, Y., Li, Y. & Zou, D. Status and opportunities in the treatment of tetracyclines from aquatic environments by metal-organic frameworks (MOFs) and MOFs-based composites. *Mater. Today Chem.* **26**, 101209 (2022).

33. Miao, Q., Jiang, L., Yang, J., Hu, T., Shan, S., Su, H., & Wu, F. MOF/hydrogel composite-based adsorbents for water treatment: A review. *J. Water Process Eng.* **50**, 103348 (2022).

34. Amin, P., Shojaei, A. & Hamzehlouyan, T. ZIF-8/Chitosan hybrid nanoparticles with tunable morphologies as superior adsorbents towards both anionic and cationic dyes for a broad range of acidic and basic environments. *Microporous Mesoporous Mater.* **343**, 112149 (2022).

35. Zhan, G. & Zeng, H. C. Hydrogen spillover through Matryoshka-type (ZIFs@) n− 1ZIFs nanocubes. *Nat. Commun.* **9**, 3778 (2018).

36. He, H., Feng, D., Zhang, X. & Feng, Y. Transport properties of ZIF-8 nanocrystals for hydrogen adsorption: Molecular dynamics study. *J. Energy Storage* **72**, 108270 (2023).

37. Almanassra, I. W., Jaber, L., Chatla, A., Abushawish, A., Shanableh, A., & Atieh, M. A. Unveiling the relationship between MOF porosity, particle size, and polyethersulfone membranes properties for efficient decontamination of dye and organic matter. *Chem. Eng. J.* **471**, 144616 (2023).

38. Liu, L., Yang, W., Gu, D., Zhao, X. & Pan, Q. In situ preparation of chitosan/ZIF-8 composite beads for highly efficient removal of U (VI). *Front. Chem.* **7**, 607 (2019).

39. Lin, W., Gong, J., Ye, W., Huang, X. & Chen, J. Polyhydroxy Fullerene-loaded ZIF-8 Nanocomposites for Better Photodynamic Therapy. *Zeitschrift für Anorg. und Allg. Chemie* **646**, 1900–1903 (2020).

40. Wang, C.-C., Li, J.-R., Lv, X.-L., Zhang, Y.-Q. & Guo, G. Photocatalytic organic pollutants degradation in metal–organic frameworks. *Energy Environ. Sci.* **7**, 2831–2867 (2014).

41. Kumar, A., Rana, S., Sharma, G., Dhiman, P., Shekh, M. I., & Stadler, F. J. Recent advances in zeolitic imidazole frameworks based photocatalysts for organic pollutant degradation and clean energy production. *J. Environ. Chem. Eng.* **11**, 110770 (2023).

42. Kong, Z. C., Liao, J. F., Dong, Y. J., Xu, Y. F., Chen, H. Y., Kuang, D. B., & Su, C. Y. Core@ shell $CsPbBr_3$@ zeolitic imidazolate framework nanocomposite for efficient photocatalytic CO_2 reduction. *ACS Energy Lett.* **3**, 2656–2662 (2018).

43. Amdeha, E. Biochar-based nanocomposites for industrial wastewater treatment via adsorption and photocatalytic degradation and the parameters affecting these processes. *Biomass Convers. Biorefinery* **14**, 23293–23318 (2024).

44. Abou-Hadid, A. F., El-Behairy, U. A., Elmalih, M. M., Amdeha, E., El Naggar, A. M., Taha, M. H., & Hussein, A. E. Production of efficient carbon fiber from different solid waste residuals for adsorption of

hazardous metals from wastewater samples. *Biomass Convers. Biorefinery* **14**, 10501–10516 (2024).

45. Abou-Hadid, A. F., El-Behairy, U. A., Elmalih, M. M., Amdeha, E., Naggar, A. M. E., Taha, M. H., & Hussein, A. E. Conversion of corn shell as biomass solid waste into carbon species for efficient decontamination of wastewater via heavy metals adsorption. *Biomass Convers. Biorefinery* **14**, 16435–16449 (2024).
46. Song, B., Lin, R., Lam, C. H., Wu, H., Tsui, T. H., & Yu, Y. Recent advances and challenges of inter-disciplinary biomass valorization by integrating hydrothermal and biological techniques. *Renew. Sustain. Energy Rev.* **135**, 110370 (2021).
47. Huo, X., Zhou, P., Zhang, J., Liu, Y., Cheng, X., Liu, Y., Li, W. and Zhang, Y. N, S-Doped porous carbons for persulfate activation to remove tetracycline: Nonradical mechanism. *J. Hazard. Mater.* **391**, 122055 (2020).
48. Olowoyo, J.O., Saini, U., Kumar, M., Valdes, H., Singh, H., Omorogie, M.O., Babalola, J.O., Vorontsov, A.V., Kumar, U. and Smirniotis, P.G. Reduced graphene oxide/NH_2-MIL-125 (Ti) composite: Selective CO_2 photoreduction to methanol under visible light and computational insights into charge separation. *J. CO_2 Util.* **42**, 101300 (2020).
49. Tian, W., Zhang, H., Duan, X., Sun, H., Tade, M. O., Ang, H. M., & Wang, S. Nitrogen-and sulfur-codoped hierarchically porous carbon for adsorptive and oxidative removal of pharmaceutical contaminants. *ACS Appl. Mater. Interfaces* **8**, 7184–7193 (2016).
50. Lee, J., Kim, K.-H. & Kwon, E. E. Biochar as a catalyst. *Renew. Sustain.*

Energy Rev. **77**, 70–79 (2017).

51. Sharma, G., Kumar, A., Naushad, M., Kumar, A., Al-Muhtaseb, A.A.H., Dhiman, P., Ghfar, A.A., Stadler, F.J. & Khan, M.R. Photoremediation of toxic dye from aqueous environment using monometallic and bimetallic quantum dots based nanocomposites. *J. Clean. Prod.* **172**, 2919–2930 (2018).
52. Stella Mary, G., Sugumaran, P., Niveditha, S., Ramalakshmi, B., Ravichandran, P., & Seshadri, S. Production, characterization and evaluation of biochar from pod (Pisum sativum), leaf (Brassica oleracea) and peel (Citrus sinensis) wastes. *Int. J. Recycl. Org. Waste Agric.* **5**, 43–53 (2016).
53. Zhang, J., Huang, D., Shao, J., Zhang, X., Zhang, S., Yang, H., & Chen, H. A new nitrogen-enriched biochar modified by ZIF-8 grafting and annealing for enhancing CO_2 adsorption. *Fuel Process. Technol.* **231**, 107250 (2022).
54. Zhang, J., Lü, F., Luo, C., Shao, L. & He, P. Humification characterization of biochar and its potential as a composting amendment. *J. Environ. Sci.* **26**, 390–397 (2014).
55. Sahoo, S. S., Vijay, V. K., Chandra, R. & Kumar, H. Production and characterization of biochar produced from slow pyrolysis of pigeon pea stalk and bamboo. *Clean. Eng. Technol.* **3**, 100101 (2021).
56. Wang, C., Yang, R. & Wang, H. Synthesis of ZIF-8/fly ash composite for adsorption of Cu^{2+}, Zn^{2+} and Ni^{2+} from aqueous solutions. *Materials (Basel).* **13**, 214 (2020).
57. Sultana, M., Mohapatra, S. R. & Ahmaruzzaman, M. A novel porous

and highly efficient Fe-Ce-Co nanoparticles anchored in biochar derived from coconut husk for photo-Fenton degradation of binary mixtures of dyes. *Environ. Nanotechnology, Monit. Manag.* **20**, 100901 (2023).

58. Bergaoui, M., Khalfaoui, M., Awadallah-F, A. & Al-Muhtaseb, S. A review of the features and applications of ZIF-8 and its derivatives for separating CO_2 and isomers of C3-and C4-hydrocarbons. *J. Nat. Gas Sci. Eng.* **96**, 104289 (2021).
59. Peng, H.-J., Zheng, P.-Q., Chao, H.-Y., Jiang, L. & Qiao, Z.-P. CdSe/ZIF-8-x: synthesis and photocatalytic CO_2 reduction performance. *RSC Adv.* **10**, 551–555 (2020).
60. Abd El Khalk, A. A., Betiha, M. A., Mansour, A. S., Abd El Wahed, M. G. & Al-Sabagh, A. M. High degradation of methylene blue using a new nanocomposite based on zeolitic imidazolate framework-8. *ACS omega* **6**, 26210–26220 (2021).
61. Eskandarloo, H., Badiei, A., Behnajady, M. A., Tavakoli, A. & Ziarani, G. M. Ultrasonic-assisted synthesis of Ce doped cubic–hexagonal $ZnTiO_3$ with highly efficient sonocatalytic activity. *Ultrason. Sonochem.* **29**, 258–269 (2016).
62. Feng, S., Jia, X., Yang, J., Li, Y., Wang, S., & Song, H. One-pot synthesis of core–shell ZIF-8@ ZnO porous nanospheres with improved ethanol gas sensing. *J. Mater. Sci. Mater. Electron.* **31**, 22534–22545 (2020).
63. Gupta, S. V., Kulkarni, V. V. & Ahmaruzzaman, M. ZIF-8 incorporated CeO_2-CdS quantum dots@ 2D g-C_3N_4 nanosheets as a staggered type II heterojunction for decolouration of a set of dyes. *J. Environ. Chem.*

Eng. **12**, 111642 (2024).

64. Sinha, T., Ahmaruzzaman, M. & Bhattacharjee, A. A simple approach for the synthesis of silver nanoparticles and their application as a catalyst for the photodegradation of methyl violet 6B dye under solar irradiation, *J. Environ. Chem. Eng.* **2** (2014) 2269–2279 (2014).

65. Liu, R. & Ou, H. T. Synthesis and Application of Magnetic Photocatalyst of Ni-Zn Ferrite/TiO_2 from IC Lead Frame Scraps. *J. Nanotechnol.* **2015**, 727210 (2015).

66. Gupta, S. V., Kulkarni, V. V & Ahmaruzzaman, M. A robust bio-source mediated CeO_2–SnS_2 quantum dots@ Oryza sativa var. biochar, photo-adsorbent for removal of Baszol Violet 571 dye from aqueous discharge: Development, materialistic analyses, and its application. *J. Water Process Eng.* **60**, 105159 (2024).

67. Mishra, S. R., Gadore, V. & Ahmaruzzaman, M. Inorganic–organic hybrid quantum dots for AOP-mediated photodegradation of ofloxacin and para-nitrophenol in diverse water matrices. *NPJ Clean Water* **6**, 78 (2023).

68. Hazarika, B., Bhattacharjee, B. & Ahmaruzzaman, M. Enhanced photocatalytic degradation of brilliant green using g-C_3N_5/WO_3 nanocomposite: a Z-scheme charge transfer approach under visible light irradiation. *Inorg. Chem. Commun.* **168**, 112960 (2024).

69. Gadore, V., Mishra, S. R. & Ahmaruzzaman, M. One-pot synthesis of CdS/CeO_2 heterojunction nanocomposite with tunable bandgap for the enhanced advanced oxidation process. *Sci. Rep.* **13**, 7708 (2023).

70. Angela, S., Lunardi, V.B., Kusuma, K., Soetaredjo, F.E., Putro, J.N.,

Santoso, S.P., Angkawijaya, A.E., Lie, J., Gunarto, C., Kurniawan, A. & Ismadji, S. Facile synthesis of hierarchical porous ZIF-8@ TiO_2 for simultaneous adsorption and photocatalytic decomposition of crystal violet. *Environ. Nanotechnology, Monit. Manag.* **16**, 100598 (2021).

71. Ahmad, W., Khan, A., Ali, N., Khan, S., Uddin, S., Malik, S., Ali, N., Khan, H., Khan, H. & Bilal, M. Photocatalytic degradation of crystal violet dye under sunlight by chitosan-encapsulated ternary metal selenide microspheres. *Environ. Sci. Pollut. Res.* **28**, 8074–8087 (2021).
72. Liu, Z., Li, Y., Li, C., Thummavichai, K., Feng, C., Li, Z., Liu, S., Zhang, S., Wang, N. & Zhu, Y. MOF-derived biochar composites for enhanced high performance photocatalytic degradation of tetracycline hydrochloride. *RSC Adv.* **12**, 31900–31910 (2022).
73. Kumari, K., Moyon, N. S. & Ahmaruzzaman, M. Environmentally sustainable fabrication of SnO_2/fly ash/biochar nanocomposite for enhanced photocatalytic performance for degradation of Ofloxacin and Rose Bengal. *Sci. Rep.* **15**, 1–24 (2025).
74. Shabna, S., Shaji, J.E., Dhas, S.S.J., Suresh, S., Aravind, A., Thomas, S.A., Vinita, V.S., Samuel, J. & Biju, C.S. Photocatalytic degradation of crystal violet using SnO_2/ZnO nanocomposite synthesized by facile sol-gel method. *J. Clust. Sci.* **35**, 597–606 (2024).
75. Aggarwal, N., Ramisetty, R., Kumar, N., Ali, D., Sharma, A., Kumar, G., Patial, P., Bala, K., Kapoor, A., Sharma, N.K. and Kaur, H. Insights into the structural, morphological, and electronic characteristics of ZnO nanoflowers: implications for efficient photocatalytic degradation of

crystal violet dye. *Opt. Quantum Electron.* **55**, 1007 (2023).

76. Manikandan, V. Efficient Photocatalytic Degradation of Crystal Violet and Rhodamine B Dyes Using RGO@ $ZnFe_2O_3$ Nanocomposite. *Strength Mater.* **55**, 167–178 (2023).

77. Ahmad, I., Abbasi, A., El Bahy, Z. M. & Ikram, S. Synergistic effect of silver NPs immobilized on Fe_3O_4@ L-proline magnetic nanocomposite toward the photocatalytic degradation of Victoria blue and reduction of organic pollutants. *Environ. Sci. Pollut. Res.* **30**, 78891–78912 (2023).

78. Chauhan, M., Kaur, N., Bansal, P., Kumar, R., Srinivasan, S., & Chaudhary, G. R. Proficient photocatalytic and sonocatalytic degradation of organic pollutants using CuO nanoparticles. *J. Nanomater.* **2020**, 6123178 (2020).

79. Kamalam, M.B.R., Inbanathan, S.S.R., Sethuraman, K., Umar, A., Algadi, H., Ibrahim, A.A., Rahman, Q.I., Garoufalis, C.S. and Baskoutas, S. Direct sunlight-driven enhanced photocatalytic performance of V_2O_5 nanorods/graphene oxide nanocomposites for the degradation of Victoria blue dye. *Environ. Res.* **199**, 111369 (2021).

80. Raha, S. & Ahmaruzzaman, M. Enhanced performance of a novel superparamagnetic g-C_3N_4/NiO/ZnO/Fe_3O_4 nanohybrid photocatalyst for removal of esomeprazole: Effects of reaction parameters, co-existing substances and water matrices. *Chem. Eng. J.* **395**, 124969 (2020).

81. Zhang, Y., Xiao, Y., Zhong, Y. & Lim, T.-T. Comparison of amoxicillin photodegradation in the UV/H_2O_2 and UV/persulfate systems: Reaction

kinetics, degradation pathways, and antibacterial activity. *Chem. Eng. J.* **372**, 420–428 (2019).

82. Santiago, D.E., Araña, J., González-Díaz, O., Alemán-Dominguez, M.E., Acosta-Dacal, A.C., Fernandez-Rodríguez, C., Pérez-Peña, J. & Doña-Rodríguez, J.M. Effect of inorganic ions on the photocatalytic treatment of agro-industrial wastewaters containing imazalil. *Appl. Catal. B Environ.* **156**, 284–292 (2014).
83. Sultana, M. & Ahmaruzzaman, M. A novel Ce-Ni@ biochar nanocomposite with enhanced photocatalytic activity towards organic dyes degradation: impact of process variables and water matrices. *Environ. Sci. Pollut. Res.* **30**, 83463–83484 (2023).
84. Yang, S., Wang, P., Yang, X., Shan, L., Zhang, W., Shao, X., & Niu, R. Degradation efficiencies of azo dye Acid Orange 7 by the interaction of heat, UV and anions with common oxidants: persulfate, peroxymonosulfate and hydrogen peroxide. *J. Hazard. Mater.* **179**, 552–558 (2010).
85. Liang, H., Li, X., Yang, Y. & Sze, K. Effects of dissolved oxygen, pH, and anions on the 2, 3-dichlorophenol degradation by photocatalytic reaction with anodic TiO_2 nanotube films. *Chemosphere* **73**, 805–812 (2008).
86. Zhang, W., An, T., Cui, M., Sheng, G. & Fu, J. Effects of anions on the photocatalytic and photoelectrocatalytic degradation of reactive dye in a packed-bed reactor. *J. Chem. Technol. Biotechnol. Int. Res. Process. Environ. Clean Technol.* **80**, 223–229 (2005).
87. Chládková, B., Evgenidou, E., Kvítek, L., Panáček, A., Zbořil, R., Kovář,

P., & Lambropoulou, D. Adsorption and photocatalysis of nanocrystalline TiO_2 particles for reactive red 195 removal: effect of humic acids, anions and scavengers. *Environ. Sci. Pollut. Res.* **22**, 16514–16524 (2015).

88. Yajun, W., Kecheng, L. U. & Changgen, F. Influence of inorganic anions and organic additives on photocatalytic degradation of methyl orange with supported polyoxometalates as photocatalyst. *J. Rare Earths* **31**, 360–365 (2013).

89. Abramović, B., Despotović, V., Šojić, D. & Finčur, N. Mechanism of clomazone photocatalytic degradation: hydroxyl radical, electron and hole scavengers. *React. Kinet. Mech. Catal.* **115**, 67–79 (2015).

90. Mohanta, D. & Ahmaruzzaman, M. Facile fabrication of novel Fe_3O_4-SnO_2-gC_3N_4 ternary nanocomposites and their photocatalytic properties towards the degradation of carbofuran. *Chemosphere* **285**, 131395 (2021).

91. Darabdhara, G., Boruah, P.K., Borthakur, P., Hussain, N., Das, M.R., Ahamad, T., Alshehri, S.M., Malgras, V., Wu, K.C.W. and Yamauchi, YReduced graphene oxide nanosheets decorated with Au–Pd bimetallic alloy nanoparticles towards efficient photocatalytic degradation of phenolic compounds in water. *Nanoscale* **8**, 8276–8287 (2016).

92. Gao, Y., Li, Y., Zhang, L., Huang, H., Hu, J., Shah, S. M., & Su, X. Adsorption and removal of tetracycline antibiotics from aqueous solution by graphene oxide. *J. Colloid Interface Sci.* **368**, 540–546 (2012).

93. Han, L., Sun, K., Jin, J., Wei, X., Xia, X., Wu, F., Gao, B. & Xing, B. Role

of structure and microporosity in phenanthrene sorption by natural and engineered organic matter. *Environ. Sci. Technol.* **48**, 11227–11234 (2014).

94. Cortés Arriagada, D., Sanhueza, L. & Wrighton, K. Removal of 4-chlorophenol using graphene, graphene oxide, and a-doped graphene (A= N, B): A computational study. *Int. J. Quantum Chem.* **113**, 1931–1939 (2013).

95. Tran, H.N., Tomul, F., Ha, N.T.H., Nguyen, D.T., Lima, E.C., Le, G.T., Chang, C.T., Masindi, V. & Woo, S.H. Innovative spherical biochar for pharmaceutical removal from water: Insight into adsorption mechanism. *J. Hazard. Mater.* **394**, 122255 (2020).

96. Rong, X., Xie, M., Kong, L., Natarajan, V., Ma, L., & Zhan, J. The magnetic biochar derived from banana peels as a persulfate activator for organic contaminants degradation. *Chem. Eng. J.* **372**, 294–303 (2019).

97. Hadi, H. J., Ammar, S. H., Mohammed, I. S. & Jabbar, Z. H. Fabrication and adsorption/photocatalytic degradation activities of (ZIF-8/Ag-$AgVO_3$) composites. *Inorg. Chem. Commun.* **163**, 112350 (2024).

98. Li, H., He, C., Xiao, A., Hu, Y., Luo, L., & Jiang, F. Dye-sensitization on rosette-shaped BiOBr/Biochar photocatalyst for simultaneous removal of emerging pollutants and dyes. *J. Clean. Prod.* **469**, 143239 (2024).

99. Nipa, S.T., Akter, R., Raihan, A., Rasul, S.B., Som, U., Ahmed, S., Alam, J., Khan, M.R., Enzo, S. and Rahman, W. State-of-the-art biosynthesis of tin oxide nanoparticles by chemical precipitation method towards photocatalytic application. *Environ. Sci. Pollut. Res.* **29**, 10871–10893

(2022).

100. Roy, S., Mishra, S. R. & Ahmaruzzaman, M. Ultrasmall copper-metal organic framework (Cu-MOF) quantum dots decorated on waste derived biochar for enhanced removal of emerging contaminants: Synergistic effect and mechanistic insight. *J. Environ. Manage.* **366**, 121802 (2024).

101. Mohanta, D. & Ahmaruzzaman, M. A novel Au-SnO2-rGO ternary nanoheterojunction catalyst for UV-LED induced photocatalytic degradation of clothianidin: Identification of reactive intermediates, degradation pathway and in-depth mechanistic insight. *J. Hazard. Mater.* **397**, 122685 (2020).

102. Swedha, M., Okla, M. K., Abdel-Maksoud, M. A., Kokilavani, S., Kamwilaisak, K., Sillanpää, M., & Khan, S. S. Photo-Fenton system Fe_3O_4/$NiCu_2S_4$ QDs towards bromoxynil and cefixime degradation: A realistic approach. *Surfaces and Interfaces* **38**, 102764 (2023).